Geophysical Prospecting, 2005, **53**, 373–397

Numerical modelling of interface scattering of seismic wavefield from a random rough interface in an acoustic medium: comparison between 2D and 3D cases

Wasiu Makinde,[1]* Nathalie Favretto-Cristini[1] and Eric de Bazelaire[2]

[1]*CNRS-FRE 2639, Imagerie Géophysique, Université de Pau et de Pays de l'Adour, BP 1155, 64013 Pau Cedex, and* [2]*11, Route du Bourg, 64230 Beyrie-en-Béarn, France*

Received June 2003, revision accepted May 2004

ABSTRACT

Seismic wavefield scattering from a statistically randomly rough interface in a multilayered piecewise homogeneous medium is studied in 3D. The influence of the surface roughness on the scattered wavefield is analysed numerically by using a finite-difference operator in the acoustic domain. Since interface scattering in the real practical sense is a 3D physical phenomenon, we show in this work that the scattering response of a randomly rough interface is not the same in 3D situations as in the 2D cases described in some earlier works. For a given interface roughness height in 3D, an interface roughness height at least three times greater is required to produce an equivalent phase scattering effect in 2D situations, for a given correlation length of the interface roughness scale. Based on observations from spectral analysis, we show that scattering results principally in de-phasing and frequency band-limiting of the incident wavefront, the frequency band-limiting properties being comparable to cases reported in the literature for absorption and thin-layer filtering. The interface scattering phenomenon should be critically considered when using amplitude and phase information from seismic signal during inversion processes.

INTRODUCTION

The amplitude and phase of seismic signal are two important parameters which are normally exploited during inversion processes in reflection seismology. In order to be able to use information from these parameters for inversion purposes, it is essential that the method for modelling the subsurface includes all the physical phenomena that affect these parameters. Interface scattering is one such important physical phenomenon almost overlooked in reflection seismology, despite its considerable impact on these parameters. It is well known that a scattering regime depends on the relationship between the wavelength and the scale of heterogeneity. In this work, we show that the effect of interface scattering becomes significant when the interface roughness height attains 1/5 of the wavelength of the incident wave ($\lambda/5$). This might result in errors which could at times be as much as 50% in the quantitative interpretation of the amplitude of reflected waves. Thus, all inversion methods using these parameters to recover the acoustic impedances or stratigraphy of the subsurface should take this important phenomenon into consideration.

Interface scattering of a seismic wavefield is associated with the spatial distributions of irregular geological contacts at the interface between layers of the stratified earth. It is well known that surface roughness is not an intrinsic property of a surface but depends on the properties of the wave that is being scattered (Ogilvy 1991). The scale of the interface roughness in relation to the wavelength of the incident wave is thus crucial in determining how energy is scattered from an interface. In optical and radar remote sensing, surfaces with roughness of the order of $\lambda/10$, where λ is the wavelength of the incident

*Now at: Total E&P Nigeria, Trans Amadi Industrial Layout, Port-Harcourt, Nigeria. E-mail: Wasiu.Makinde@total.com

wave on the surface, are generally considered smooth. The Rayleigh criterion (Ishimaru 1978) takes the limit or threshold for the smoothness of a surface to be $h < \lambda/8\cos\theta$, where h represents the surface height roughness (root-mean-square (rms) height) and θ is the angle of incidence. Consequently, if we assume a plane wave at normal incidence and use the $\lambda/10$ criterion, then for the seismic frequency bandwidth range ($10 \leq f \leq 60$ Hz) and the P-wave velocity range often encountered ($1500 \leq v \leq 5000$ m/s), surfaces with a roughness height less than the values in the range between 3 m and 50 m are considered smooth in seismic reflection surveys. Most geological surfaces are considered to be seismically 'smooth'. Nevertheless, many natural occurrences are exceptions to this limit and thus the effects of interface scattering must be taken into consideration in realistic earth models.

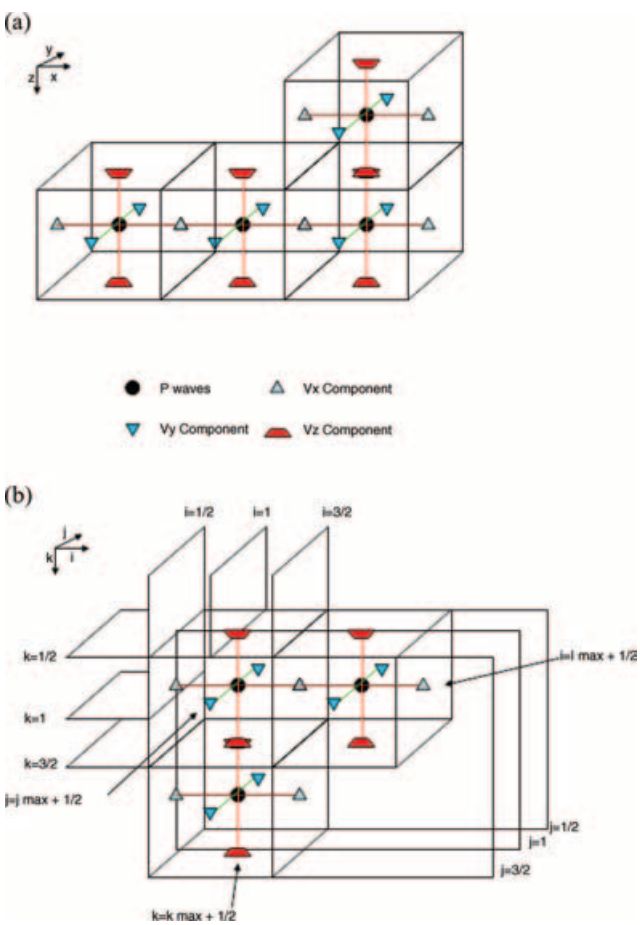

Figure 1 Grid sampling used in the discretization of the equations with the 3D mesh: (a) shows the cubic grids which constitute the 3D mesh; these can be shifted in one or many directions to obtain the staggered grid formalism of Virieux (1986). The blackened nodes are computed at time t while the other nodes are computed at times $t + \frac{1}{2}$; (b) shows the grid node indexing employed. The pressure nodes are represented in solid black in both cases.

Irregular interfaces could be created by the disruption of sedimentary layers as pre- or post-depositional deformation features. This can occur when a palaeo-relief is covered by a more recent sedimentary layer with velocities different from the adjacent layers, as is the case with angular unconformities. It also occurs in the case of certain mobile shale/sediment interfaces along shale domes and salt/sediment interfaces along salt domes and salt roofs below overhangs, often encountered in deltaic environments. Another important case worth mentioning is that of volcanic eruption (basalt). Highly rugose interfaces are the result of primary and secondary erosion processes, of jointing due to shrinkage during cooling, of vesicles due to degassing, of baking effects or of lava filling previous topography. Furthermore, consecutive deposition and erosion can amplify the relief up to a hectometre scale. These interfaces are encountered in both land and marine environments, and are known to constitute major imaging problems. The weathered zone is a well-known scatterer in land seismic data and it is known to be highly spatially irregular. Interface scattering could affect the phase and/or amplitude of the incident wavefield (Favretto-Cristini and de Bazelaire 2003), and is detrimental to the final seismic image when true/preserved amplitude imaging is being considered.

The extent to which interface roughness affects wave scattering behaviour has been the subject of studies in many fields, for example, electromagnetics, ground-penetrating radar, medicine, etc. However, the general understanding of scattering of seismic waves from highly irregular boundaries is limited because of theoretical and experimental difficulties (Schultz and Toksöz 1993). The theoretical difficulty arises from surface interactions, resulting in non-linear mathematical formulations and computationally intensive algorithms. Experimentally, the non-linearity manifests itself as multiple scattering. This multiple scattering is not easy to analyse in a simple fashion because scattered waves propagate along many complex paths. For these reasons, most earlier works have focused on detailed investigation of very specific interface structures, limited mostly to 2D cases and sometimes to 2.5D configurations. For example, Kawase (1988) used boundary elements to study the scattering of surface waves in a semicircular canyon. Bouchon, Campillo and Gaffet (1989) used discrete wavenumbers to investigate scattering of SH-waves between layers in 'synclines' and 'anticlines'. Axilrod and Ferguson (1990) studied SH-wave scattering from a sinusoidal grating using various discrete wavenumber techniques. Schultz and Toksöz (1991) used finite-differences and laboratory model-tank experiments to study the scattering from randomly distributed grooves. Schultz and Toksöz (1993)

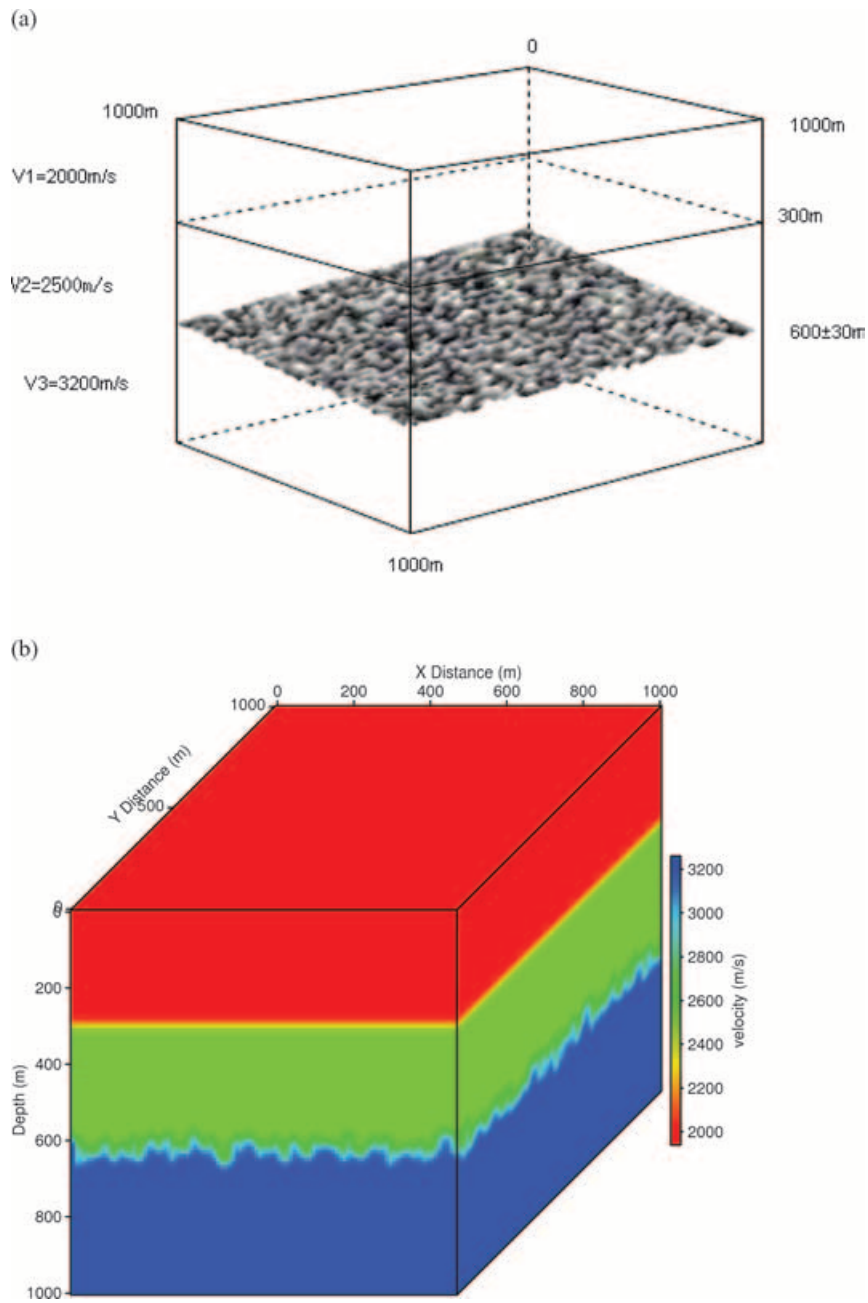

Figure 2 Simple three-layered earth model used for the numerical simulations in the 3D case: (a) is a skeletal representation of the model revealing the nature of the scattering interface in 3D; (b) shows a realization of the 3D model with surface rms height of 40 m.

also studied the enhanced backscattering of SH-waves from a highly irregular random interface to show that, in parallel with what is observed in optics, enhanced backscattering results directly from multiple scattering, and its character varies significantly as a function of impedance contrasts, incident angle and rms slope of the interface. Martini and Bean (2002) studied the effect of interface scattering from a fractal basalt environment and applied wave-equation datuming in an attempt to remove it.

Since the number of degrees of freedom required to model a 3D surface is proportional to the surface area, numerical simulation of a general 3D rough surface scattering problem is computationally expensive (Warnick and Chew 2001). This is the main reason why, in some earlier works, the simplification of translationally invariant surfaces is often used to reduce the computational cost. This, however, requires the use of earth models that are not geologically realistic. Translationally invariant surfaces (for example, corrugated surfaces where the

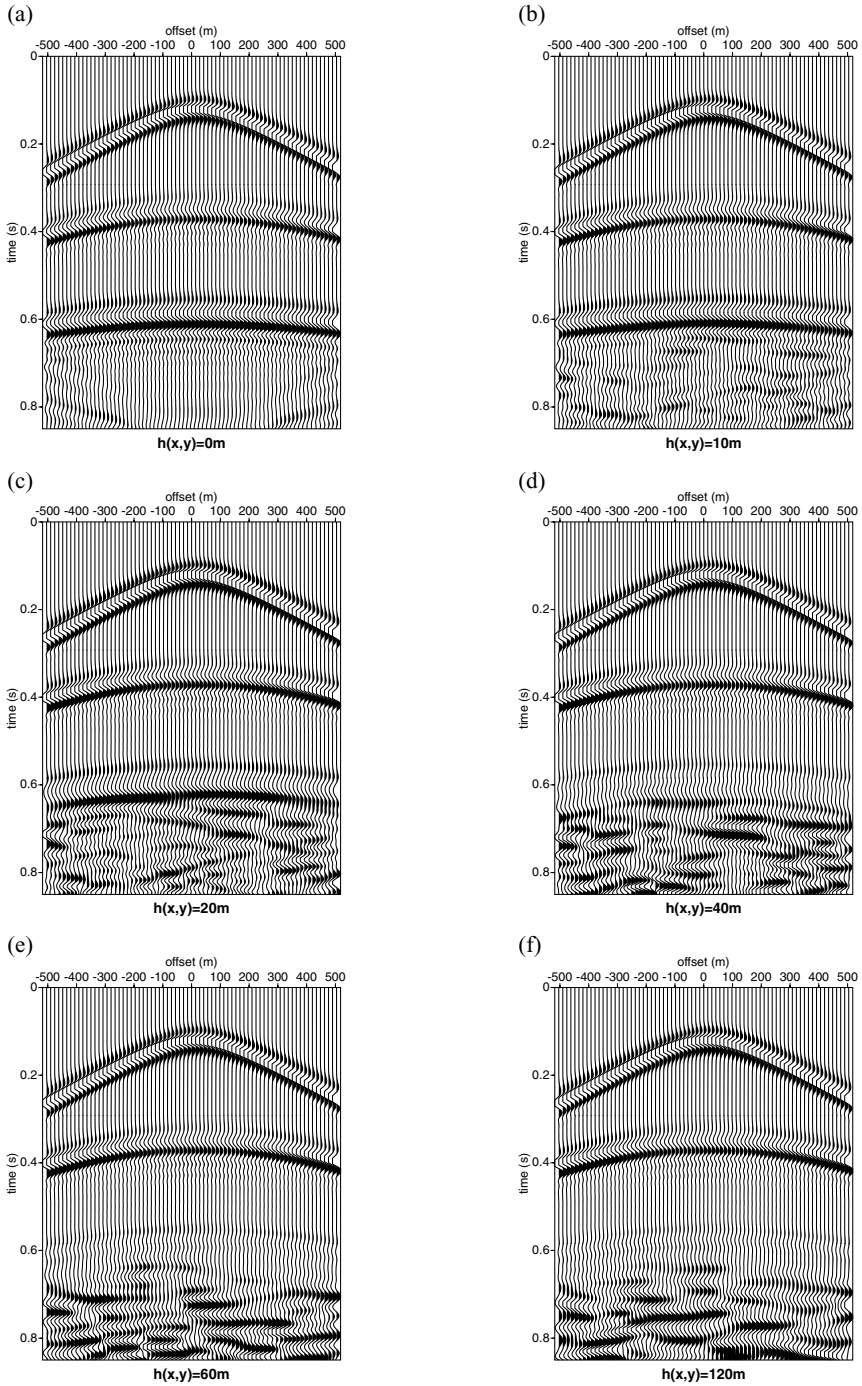

Figure 3 Receiver group data extracted from 3D data cube. The data refer to computations for different surface rms height values $h(x, y)$: (a) 0 m, (b) 10 m, (c) 20 m, (d) 40 m, (e) 60 m and (f) 120 m, for the 3D case. The computation with $h(x, y) = 0$ corresponds to the reference model (no phase scattering observed).

surface roughness varies only in one direction and is invariant in the other) do not occur in nature, and since interface scattering is a 3D phenomenon, the understanding of seismic wavefield scattering from a 3D random rough surface becomes crucial. We present a numerical study of the interface scattering of a seismic wavefield from a 3D random rough interface and compare the results with the corresponding 2D case. We employ a finite-difference operator in the acoustic domain to simulate wave propagation in a multilayered medium with a rough random interface, generated by perturbing a plane interface with a Gaussian random function. The effect of the surface height on the properties of the seismic wavefield scattered from the randomly rough interface is studied. This provides information on the way the interface scattering affects

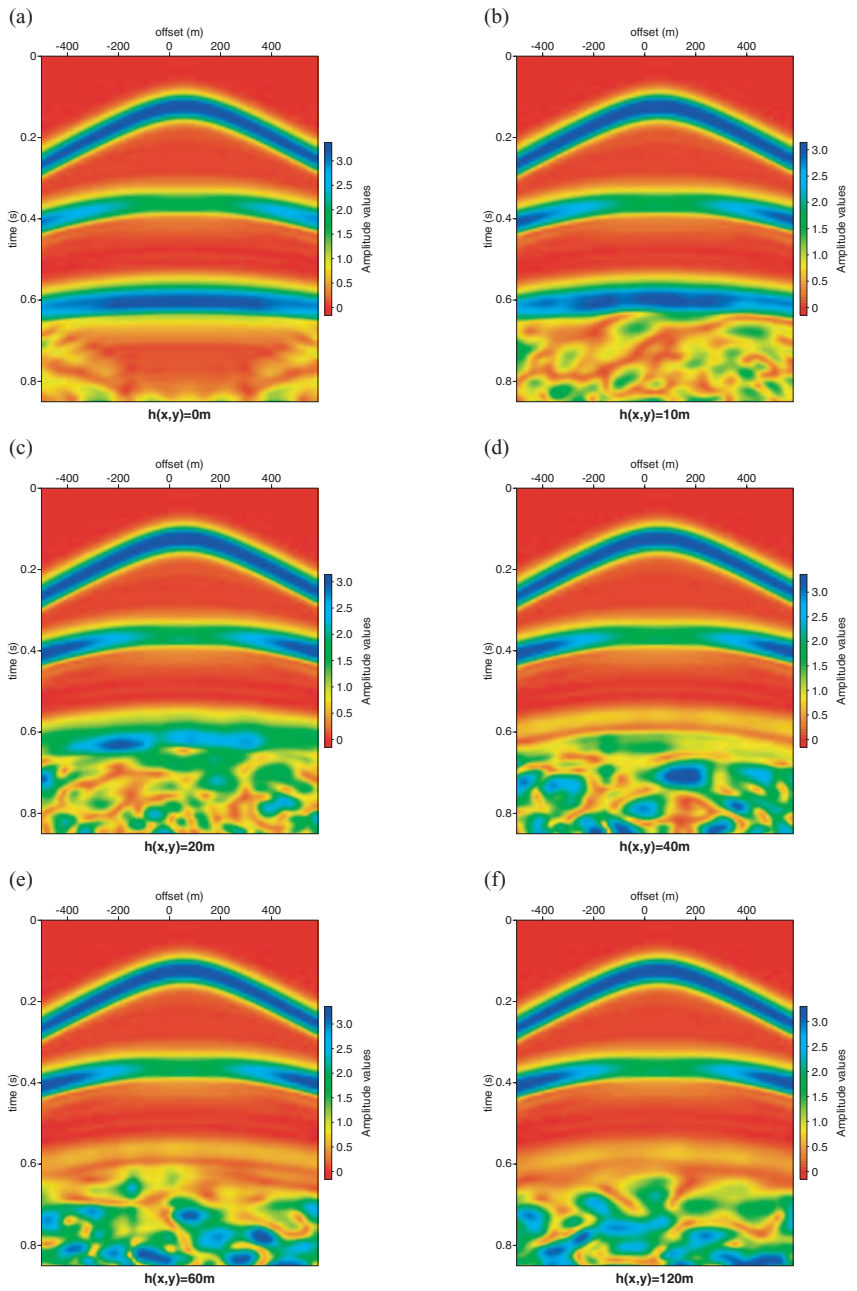

Figure 4 Instantaneous amplitude computed by the Hilbert transform method (envelope) on the synthetic data shown in Fig. 3.

the quality of the final seismic image. Comparative studies between the 2D and the 3D cases also show that the seismic response of random rough surfaces is not the same in 2D and 3D situations.

NUMERICAL ANALYSIS

Statistical description of the interface roughness

A rough interface is usually described in terms of its deviation from a 'smooth' reference surface. The shape and location of the reference surface are chosen according to the long-range behaviour of the surface. Essentially, two aspects of the nature of random rough surfaces are usually considered: the spread of the heights about the reference surface, and the variation of these heights along the surface. Statistical methods employed to describe rough surfaces are beyond the scope of this paper; however, a comprehensive list of descriptive methods and their significance can be found in Ogilvy (1991).

If the interface between two adjacent layers with different elastic/acoustic properties is statistically rough, we can

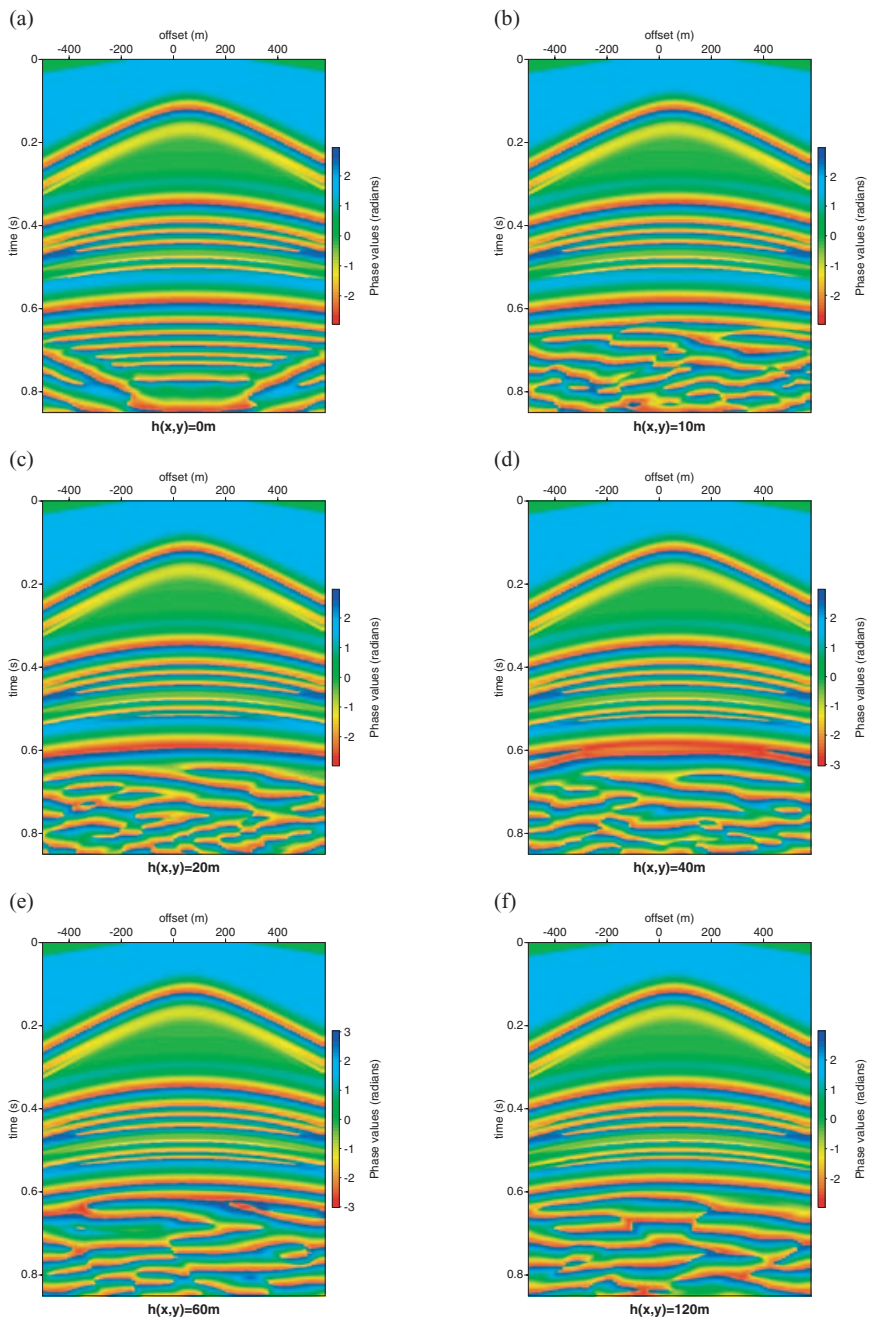

Figure 5 Phase spectrum computed for the data shown in Fig. 3.

describe such an interface by the relationship,

$$h = \xi(\mathbf{r}), \tag{1}$$

where h represents the depth in the model, $\mathbf{r}$ is a 2D vector lying in the $(x, y, 0)$-plane, and $\xi(\mathbf{r})$ is, in our case, a Gaussian random function with zero mean and a correlation function given by

$$\left\langle \xi(\mathbf{r})\xi(\mathbf{r}') \right\rangle_s = C(\mathbf{r} - \mathbf{r}'). \tag{2}$$

The brackets $\langle \ldots . \rangle_s$ indicate averaging over the realization of the random function ξ. Although anisotropy occurs in nature in such a way that geological surfaces may possess surface azimuthal anisotropy, surfaces created by stochastic processes are usually stationary and statistically isotropic, having statistical characteristics independent of the azimuth. For the purpose of our analysis, we considered a statistically isotropic 3D random interface. Consequently, the correlation function distribution is independent of the azimuth along such a surface.

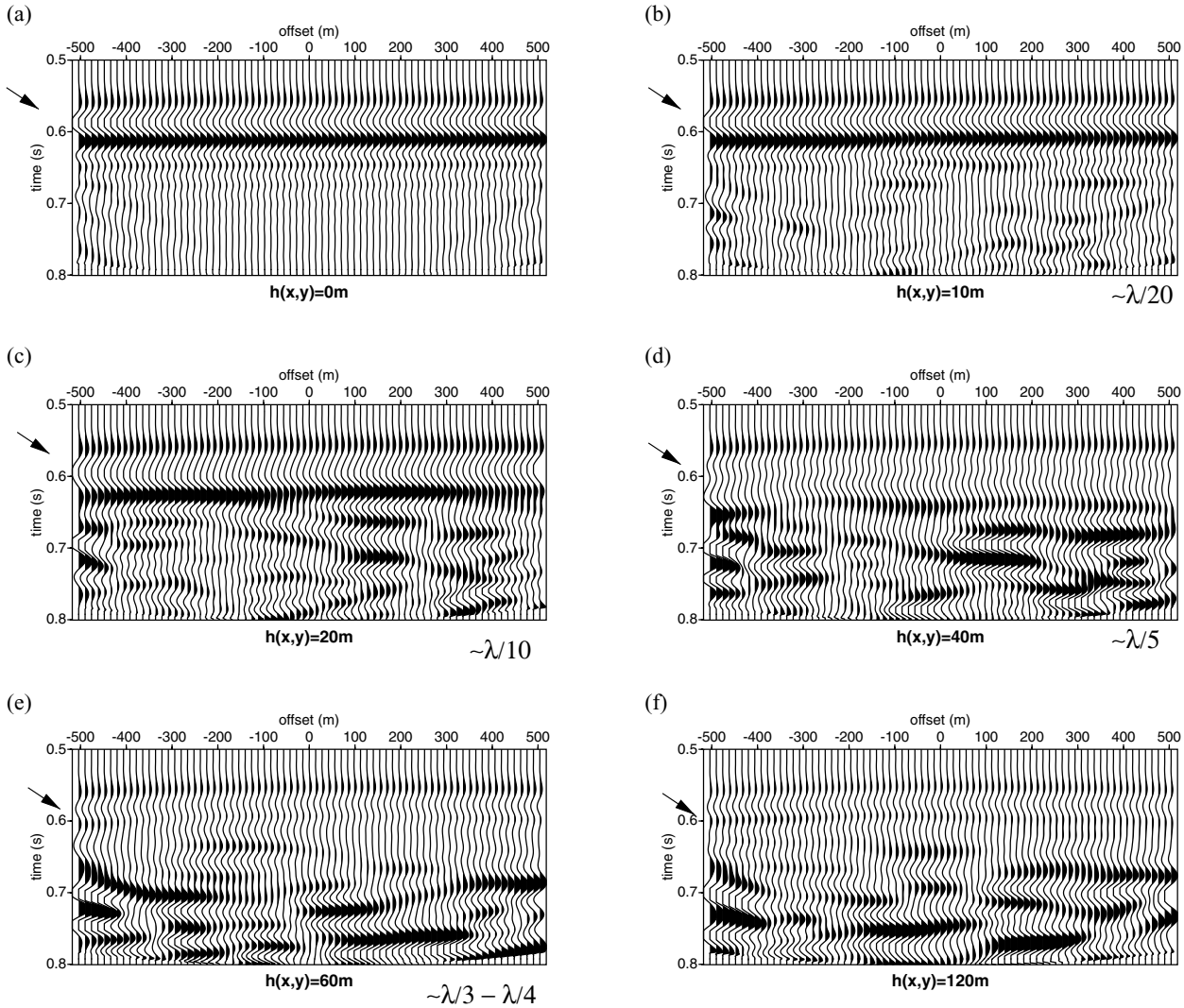

Figure 6 The seismic response of the second interface in the models after moveout correction to flatten the events for all offset ranges. This interface is a reflector for the reference model (a). It is a scattering interface in the other models: (b) $h(x, y) = 10$ m, (c) $h(x, y) = 20$ m, (d) $h(x, y) = 40$ m, (e) $h(x, y) = 60$ m, (f) $h(x, y) = 120$ m. The reflection appears at 0.6 s for the reference model (a). For increasing surface heights (b)–(f), the reflected event 'disappears' as the incident energy is gradually converted to scattered energy that is delayed on the section.

The roughness could take different values of the order of the wavelength of the propagating seismic signal in the medium above the scattering interface ($h/\lambda_c = 0.0, 0.048, 0.096, 0.192, 0.288$ and 0.576). Here, h is the rms height of the surface and λ_c is the central wavelength of the propagating seismic wave. A correlation length of 50 m was chosen to be independent of the azimuth on the surface.

Numerical scheme

We developed a 3D centred finite-difference numerical scheme in the acoustic domain based on the staggered grid formalism of Virieux (1986). This involved discretization of the hyperbolic system of the equations expressing the conservation of mass and hydrodynamics, by a first-order scheme at the nodes of a 3D mesh. This mesh was composed of cubic grids shifted by a half-mesh in one or many directions (Fig. 1a). Although the computational grids are cubic, the grid sampling was carefully chosen such that the interface distribution was well sampled in the three directions and was very much less than the correlation length of the interface distribution function. This procedure permits the computation of the pressure fields at the nodes at the centre of each cube in the grid, and the x-, y- and z-components of the velocity at nodes at the centre of each

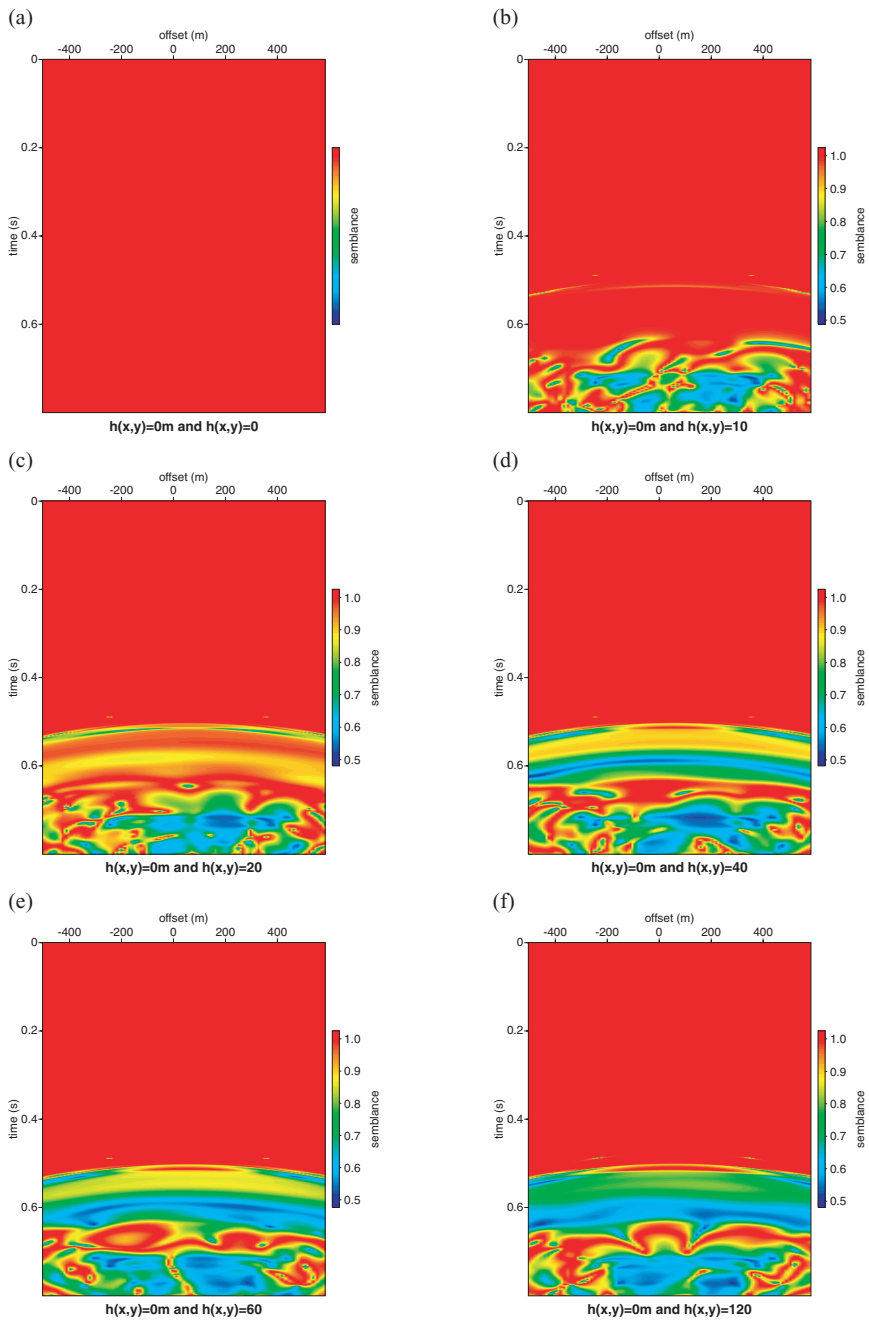

Figure 7 Computed semblance on the envelope between the reference model data and the data computed for the different surface height roughnesses of the 3D models. This gives a measure of the observed effect of phase scattering. (a) $h(x, y) = 0$ m versus $h(x, y) = 0$ m, (b) $h(x, y) = 0$ m versus $h(x, y) = 10$ m, (c) $h(x, y) = 0$ m versus $h(x, y) = 20$ m, (d) $h(x, y) = 0$ m versus $h(x, y) = 40$ m, (e) $h(x, y) = 0$ m versus $h(x, y) = 60$ m and (f) $h(x, y) = 0$ m versus $h(x, y) = 120$ m.

cube face. For the purpose of our analysis, we only considered the pressure field. To ensure the accuracy of the computed results, spurious reflections off the absorbing boundaries were avoided by padding the computational grid with an encasing spongy layer since these absorbing boundaries were only approximate.

The wave propagation in a 3D acoustic medium is governed by a system consisting of the equation of conservation of mass and the hydrodynamic equation. These equations can be written respectively as

$$\frac{\partial P}{\partial t}(x, y, z, t) - \rho(x, y, z, t)c^2(x, y, z, t)\mathrm{div}(\mathbf{v}(x, y, z, t)) = c^2(x, y, z)g(x, y, z, t) \tag{3}$$

and

$$\rho(x, y, z)\frac{\partial \mathbf{v}}{\partial t}(x, y, z, t) - \nabla P(x, y, z, t) = \mathbf{f}(x, y, z, t), \tag{4}$$

where P is a scalar function representing the pressure and $\mathbf{v}$ is the velocity vector in the medium at each point (x, y, z) in

Table 1 Spectral characteristics of the trace, obtained from the trace of the computed data for the 3D reference model

Parameters	Input signal	Interface 1	Interface 2
Frequency limits (Hz)	0–51	0–51	0–51
Carrier frequency (Hz)	20.23	20.90	20.00
Spectral eccentricity	0.300	0.272	0.271
Spectral bandwidth	44.65	44.32	44.54

Table 2 Spectral characteristics of the trace, extracted from the trace of the computed data of the 3D scattering model for a surface height of 40 m

Parameters	Input signal	Interface 1	Scattering interface
Frequency limits (Hz)	0–51	0–51	0–49
Carrier frequency (Hz)	20.42	20.05	22.60
Spectral eccentricity	0.293	0.300	0.183
Spectral bandwidth	44.48	44.83	42.19

space at each instant t of time, ρ is the density and c is the velocity of wave propagation at point $(x, y, z) \in \Re^3$. g and $\mathbf{f}$ represent, respectively, the source term and the external force field.

Considering that the medium is a closed system with no external force field, the system of equations (3) and (4) gives the following system of partial derivative equations:

$$\frac{\partial P}{\partial t} = c^2 \rho \mathrm{div}\mathbf{v} - c^2 g, \tag{5}$$

$$\frac{\partial v_x}{\partial t} = \frac{1}{\rho}\frac{\partial P}{\partial x}, \qquad \frac{\partial v_y}{\partial t} = \frac{1}{\rho}\frac{\partial P}{\partial y}, \qquad \frac{\partial v_z}{\partial t} = \frac{1}{\rho}\frac{\partial P}{\partial z}. \tag{6}$$

The above system of partial differential equations was discretized by employing the centred finite-difference scheme. If we take the spatial sampling in the three Cartesian coordinates (x, y, z) to be respectively Δx, Δy, Δz, and i, j, k, t to be the discretization indices on the x-, y-, z-axes and the time axis respectively, we can write the discretized equations as follows:

$$\begin{aligned} P^t_{i,j,k} = P^{t-1}_{i,j,k} + \Delta t (C^2 R)_{i,j,k} \Bigg\{ & \frac{1}{\Delta x}\left[U^{t-1/2}_{i+1/2,j,k} - U^{t-1/2}_{i-1/2,j,k}\right] \\ & + \frac{1}{\Delta y}\left[V^{t-1/2}_{i,j+1/2,k} - V^{t-1/2}_{i,j-1/2,k}\right] \\ & + \frac{1}{\Delta z}\left[W^{t-1/2}_{i,j,k+1/2} - W^{t-1/2}_{i,j,k+1/2}\right]\Bigg\} - \Delta t C^2_{i,j,k} G^{t-1/2}_{i,j,k}, \end{aligned} \tag{7}$$

where $P^t{}_{i,j,k}$ and $G^t{}_{i,j,k}$ represent the values of p and g, respectively, at the nodes $i\Delta x$, $j\Delta y$, $k\Delta z$ at instant t. $R_{i,j,k}$ and $C_{i,j,k}$ represent the values ρ and c respectively at the nodes $i\Delta x$, $j\Delta y$, $k\Delta z$, while $U^{t-1/2}_{i-1/2,j,k}$, $V^{t-1/2}_{i,j-1/2,k}$, $W^{t-1/2}_{i,j,k+1/2}$ represent the values of v_x, v_y and v_z respectively at the grid nodes and are time-indexed. Figure 1(b) shows examples of grid sampling and grid node indexing employed for the discretization of the equations.

The upper surface of the model was taken to be a zero-displacement surface (homogeneous Dirichlet-type boundary condition), while an absorbing condition was implemented at the other edges. The scattering interface (also the internal interfaces) was not treated with explicit boundary conditions because they are expressed in a homogeneous formulation (Kelly *et al.* 1976). They were represented as changes in velocity and density (acoustic parameters) as these quantities are expressed in a heterogeneous formulation. The problem of multiple scattering was thus implicitly addressed.

To verify the accuracy of the solution produced by the numerical scheme, we benchmarked the computation on a reference model with three horizontal plane interfaces. The traveltimes and amplitudes computed were compared with those calculated theoretically and were found to agree exactly. Since this model also serves as the reference model for the interface scattering analysis, we chose the acoustic parameters to be identical to those of the models used for the scattering studies.

Description of the 3D and 2D models

The models used for this study are simple piecewise stratified cubes consisting of three layers (Figs 2a, b) of dimensions 1000 m × 1000 m × 1000 m with interval velocities of 2000 m/s, 2500 m/s and 3200 m/s. The scattering interface was located at the base of the second layer with a velocity of 2500 m/s. The rms height of the scattering surface had values 0 m, 10 m, 20 m, 40 m, 60 m and 120 m for the simulations. An explosive source characterized by a first-order Ricker wavelet was used as the input signal. Considering a seismic signal of central frequency 12 Hz and a velocity 2500 m/s, the central wavelength in the medium above the scattering interface was about 208 m. Thus the scattering model with surface rms height of 20 m corresponds to the limit of the $\lambda/10$ criterion. The surface correlation length of 50 m was chosen with the height distribution totally independent of azimuth, thus attaining a statistically isotropic surface.

The scattering surface was generated with a random function creating a point distribution that has a Gaussian probability distribution function with zero mean. The Gaussian distribution was preferred rather than other types of

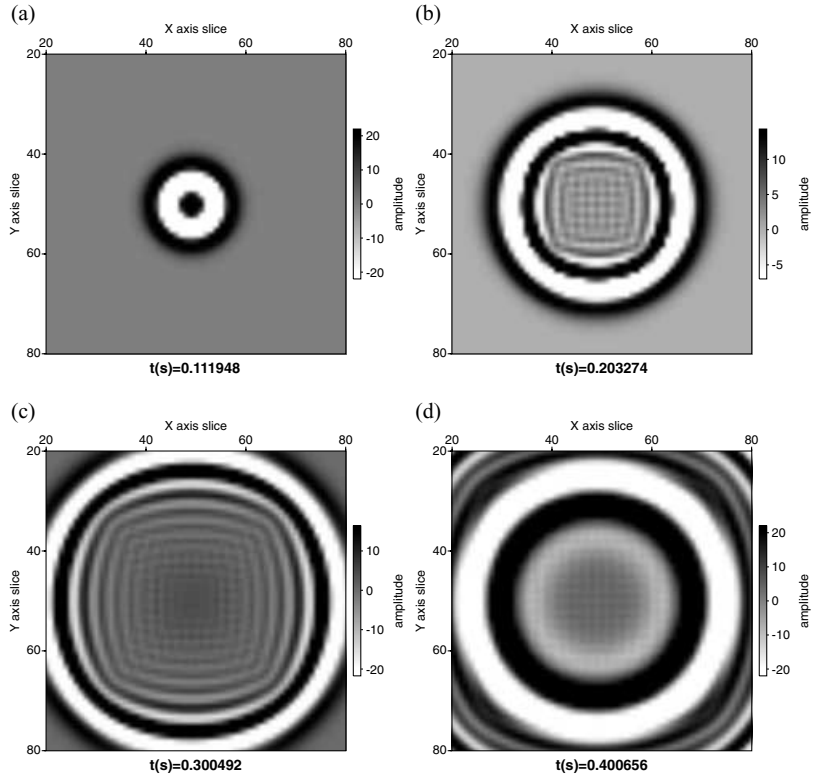

Figure 8 Snapshots of wave propagation in the 3D medium below the source at the (x, y, 0)-plane at different time-steps for the model with a surface height of 40 m. The reflection from the first interface (smooth) is at about 0.4 s (d).

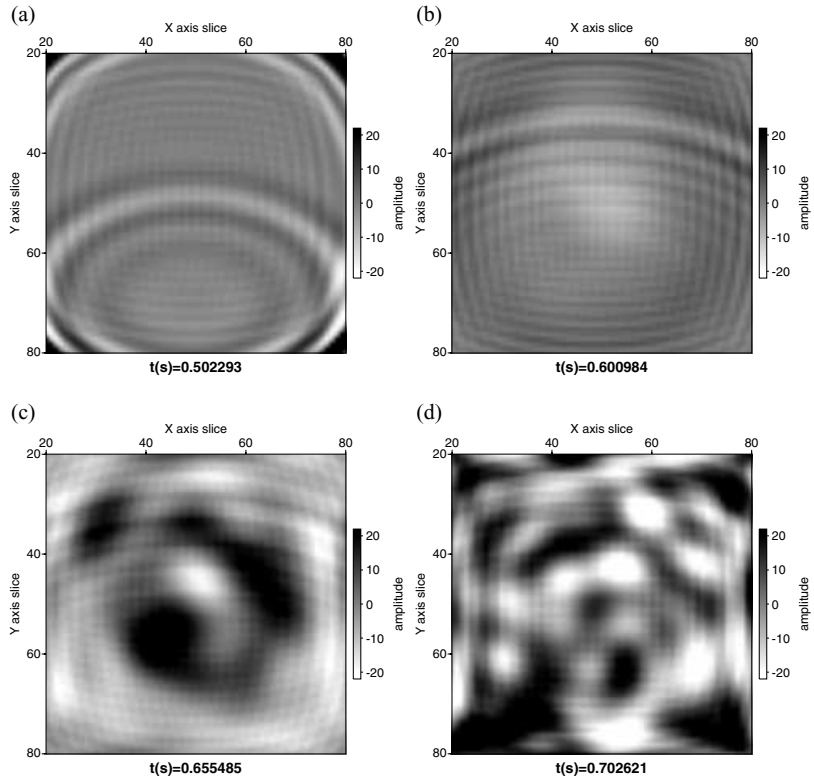

Figure 9 Snapshots of wave propagation in the 3D medium below the source. Note the phase change as the wavefield reaches the scattering interface between 0.6 and 0.7 s (c) and (d).

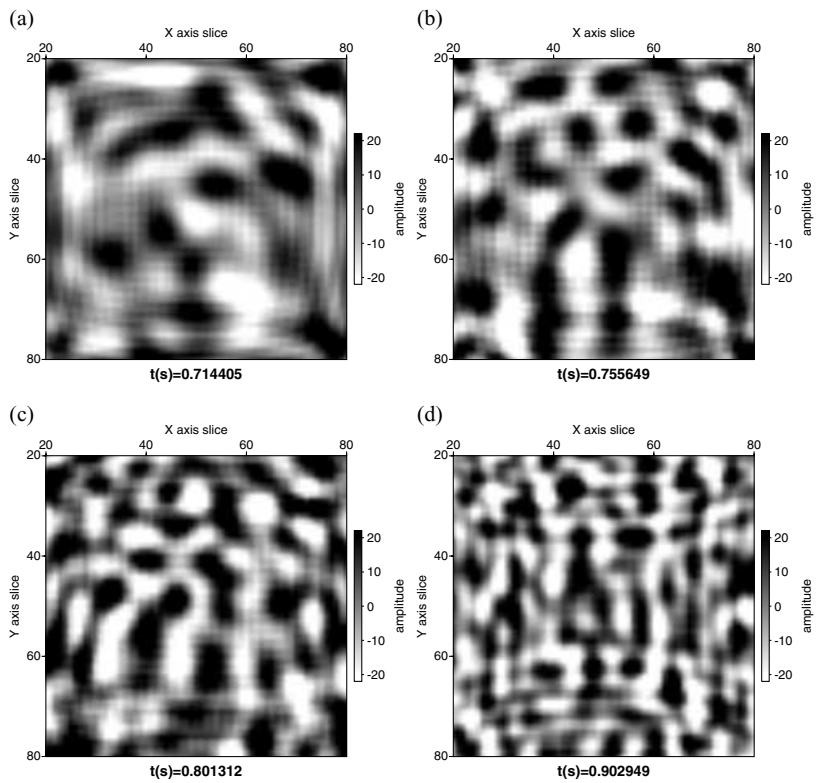

Figure 10 Snapshots of wave propagation in the 3D medium. Note that the response becomes more random after the scattering interface.

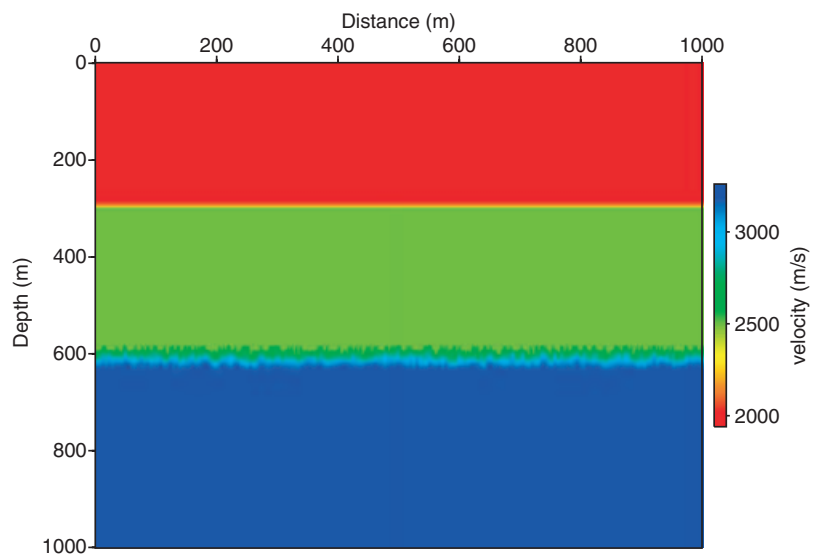

Figure 11 An example of a 2D model with a surface height of 40 m. This represents a slice in the $(x, y, 0)$-plane of the 3D model having the same surface height.

probability distribution (exponential for example) because most natural stochastic processes are better described with a Gaussian distribution. Moreover, the determination and computation of the related statistical parameters for Gaussian functions is relatively simple. Gaussian random deviates could be generated by performing a Box–Muller transform operation on uniform deviates (Box and Muller 1958). The probability distribution of such a distribution is given by

$$\Pi(h)\mathrm{d}(h) = \frac{1}{\sqrt{2\pi}} \exp\left(-\frac{h^2}{2\sigma^2}\right) \mathrm{d}h, \tag{8}$$

where $h = h(x, y)$ is the surface height distribution function. This implies that the number of points below and above the reference plane are equal. In such a case, the surface height

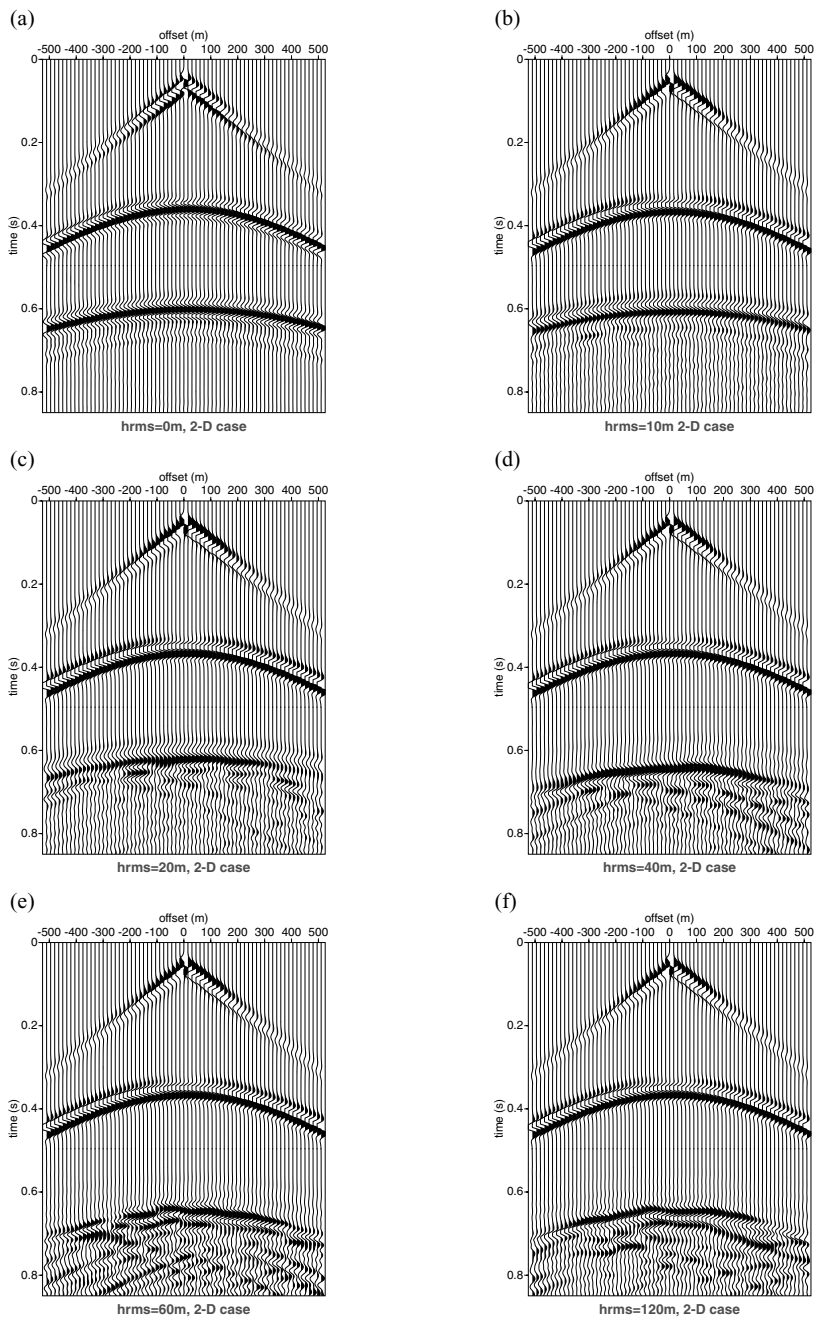

Figure 12 Simulations on 2D models with different rms heights. Simulations were realized for surface rms heights of (a) 0 m, (b) 10 m, (c) 20 m, (d) 40 m, (e) 60 m and (f) 120 m.

function satisfies the relationship,

$$\langle h \rangle_{\mathrm{s}} = \int_{-\infty}^{\infty} h \Pi(h) \mathrm{d}h = 0, \tag{9}$$

such that the rms height of the distribution equals the standard deviation and is given by

$$\sigma^2 = \sqrt{\langle h^2 \rangle_{\mathrm{s}}}, \tag{10}$$

where σ^2 is the variance. The correlation function of such a distribution is given by

$$C(\mathbf{r}) = \frac{\langle h(r) h(r + \mathbf{r}) \rangle_{\mathrm{s}}}{\sigma^2} = \exp\left(\frac{\mathbf{r}^2}{l_0}\right), \tag{11}$$

where l_0 is the correlation length of the distribution, r is a scattering point away from the surface, $\mathbf{r}$ is the vector separating two points and h is the surface height function. The variance determines the height variation of the interface while the

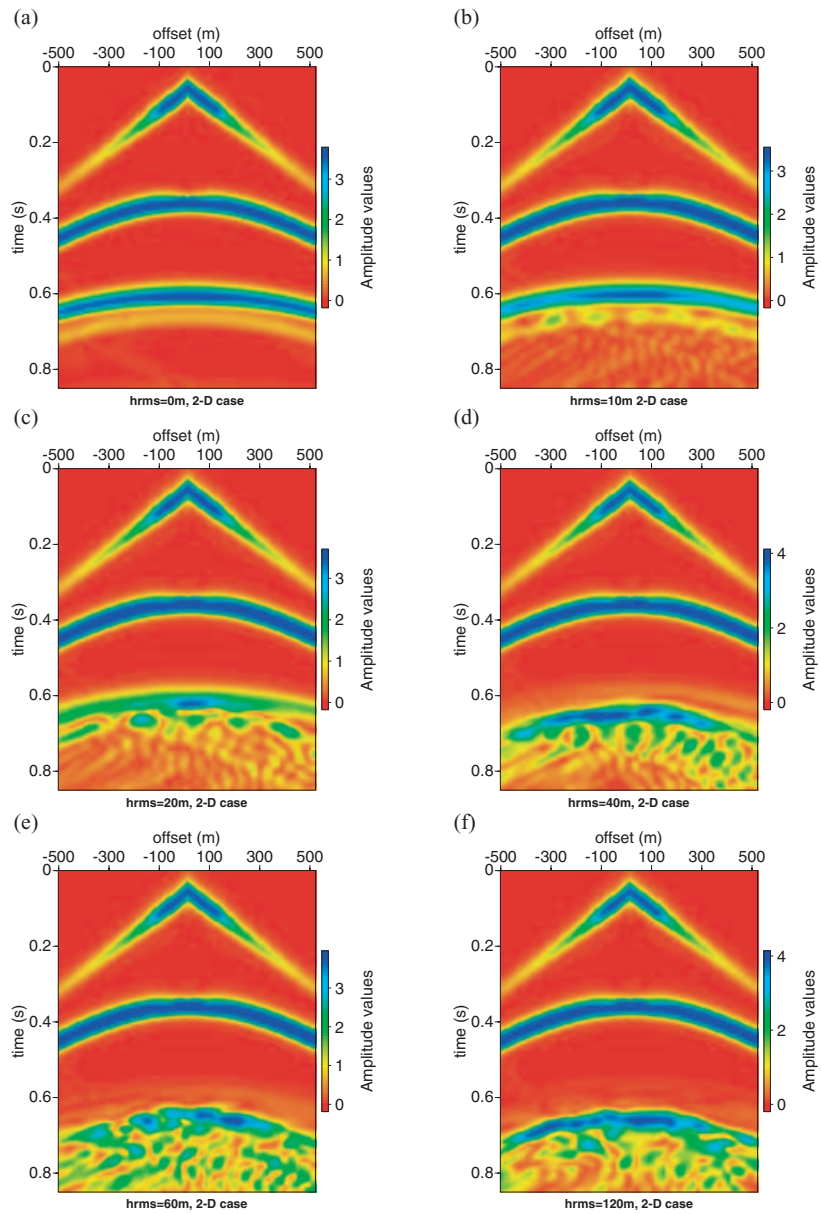

Figure 13 Instantaneous amplitude (envelope) computed with the Hilbert transform on the synthetic data from the 2D simulations of Fig. 12.

correlation length determines the maximum spatial frequency, or the lowest spatial wavelength in the surface distribution. The spatial spectrum of the interface function is the Fourier transform of the autocovariance function (non-normalized autocorrelation function) given by

$$\Psi(\mathbf{k}) = \frac{\sigma^2}{2\pi} \int C(\mathbf{r}) e^{i\mathbf{kr}} d\mathbf{r}, \tag{12}$$

where $\mathbf{k}$ is a unit vector in the z-direction.

For each simulation, we placed a network of receivers at the surface of the model. Since a homogeneous Dirichlet-type boundary was implemented at the upper surface of the model, a buried source at depth 60 m positioned at the centre was used. This accounts for the time delay observed on the computed data. The receiver spacing in the x- and y-directions was 15 m, thus giving a network of 66 × 66 traces in both x- and y-directions for a 1 km^2 acquisition. The total simulation time was 0.8 s. This configuration records the total field in the stratified medium.

For comparative studies, we also realized equivalent 2D models which correspond to slices at the middle of the 3D models (in the $(x,0,z)$-plane) with rms heights of the surface of

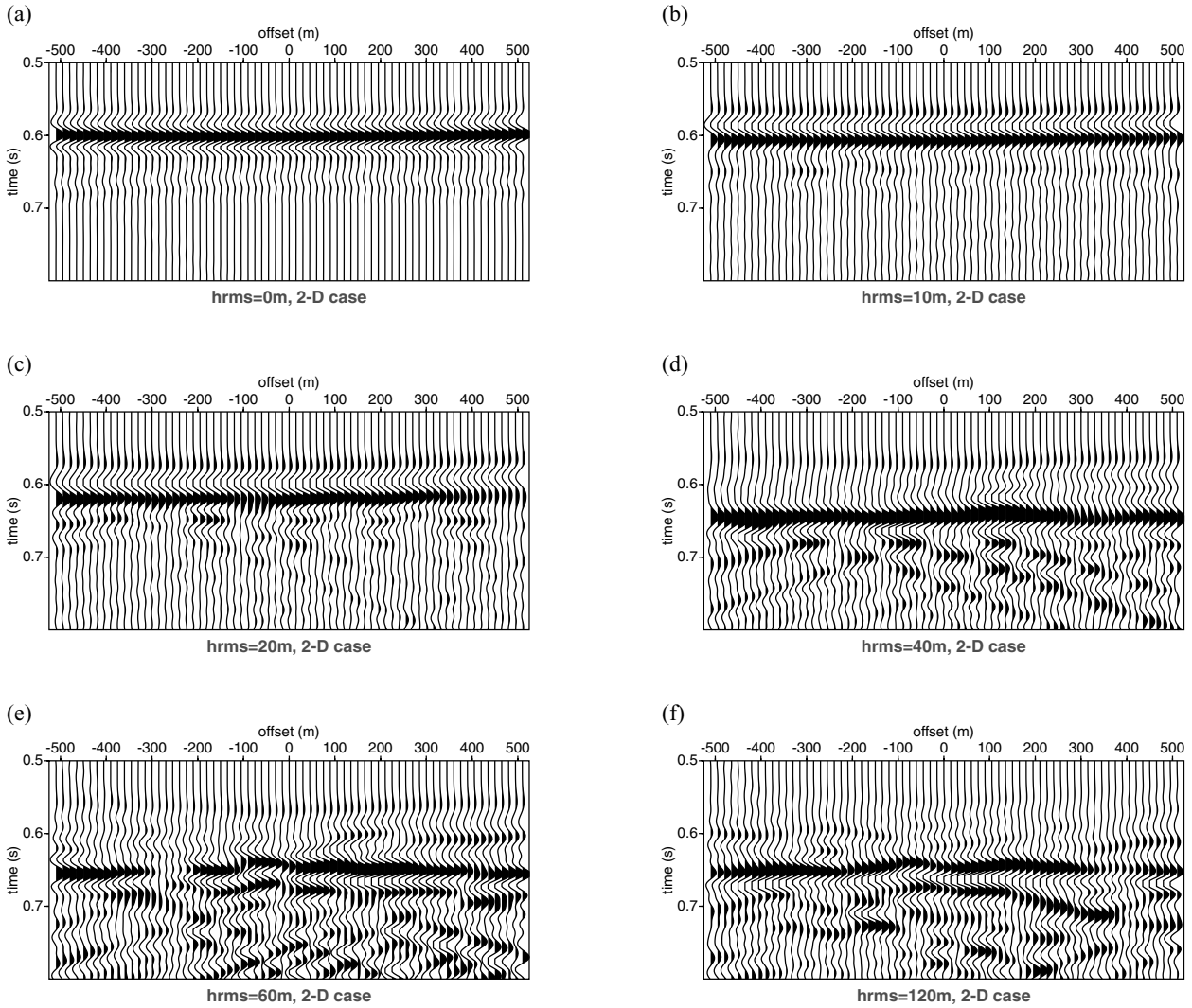

Figure 14 As Fig. 6 but for 2D simulations. Note the continuity of the events for all computed data and the relatively weak phase scattering compared with the 3D case.

0 m, 20 m, 40 m, 60 m and 120 m. These models were used for comparisons between the 2D and 3D situations for phase scattering studies.

NUMERICAL RESULTS AND DISCUSSION

In this section, we present the results of the numerical simulations on the 3D and 2D models, which are the solutions to the forward scattering problem. Firstly, we analyse the results of the 3D simulations. We then compare the 3D case with the 2D case and finally calibrate the 2D results with the 3D results. In our discussion, we refer to the effect of the interface scattering phenomenon of seismic signal on the phase of the signal as phase scattering or de-phasing. Analysis of the results of the 3D simulations is carried out on the extracted central group of the computed 3D data cube. This is a slice in the (x, t)-plane of the data cube. Since the 3D rugose interface employed for the simulations is statistically isotropic, significant discrepancies are not expected in the results of the computed data with respect to azimuth.

3D case

Figures 3(a–f) obtained from the extracted receiver groups from the centre of the simulated data cube (a slice in the (x, t)-plane) represent the simulated pressure field in the 3D medium where either no scattering interface (a), considered as the reference model, or a scattering interface with surface height of

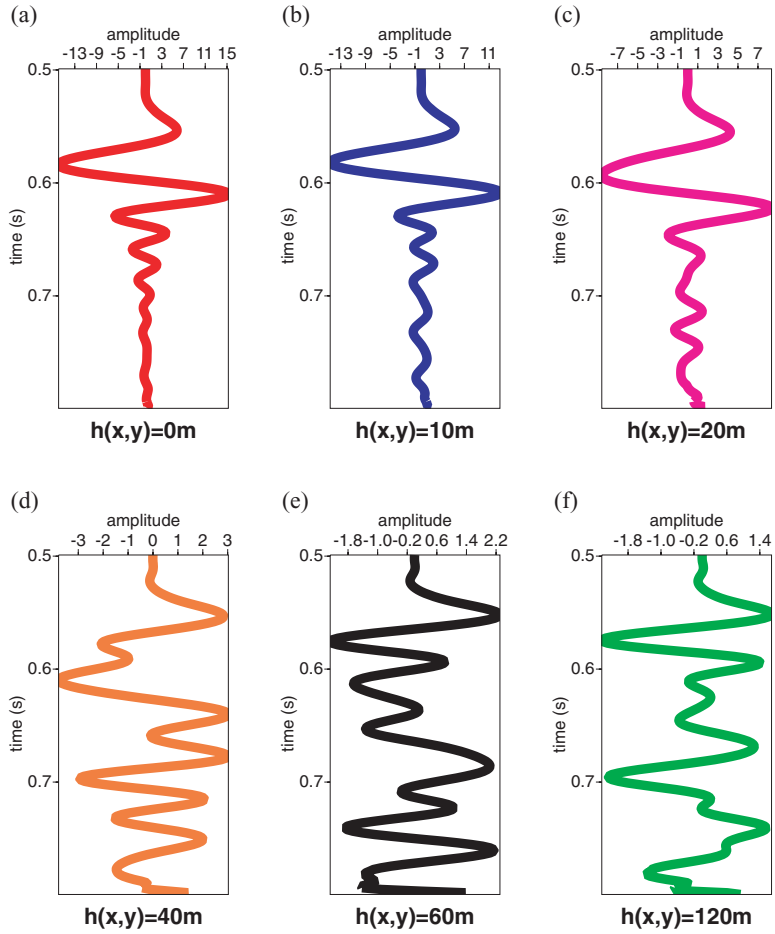

Figure 15 Stacked traces of the 3D data of Fig. 6.

(b) 10 m, (c) 20 m, (d) 40 m, (e) 60 m or (f) 120 m occurs. For the reference model $h(x, y) = 0$ m, the direct arrival and the response of the two plane interfaces are clearly discernible at zero-offset times of about 0.1 s, 0.4 s and 0.6 s, respectively. Parasitic corner reflections arising from corners of boundaries can be seen, with a very weak amplitude. These, however, do not fundamentally affect the results as they are less than 5% of the amplitude and within the acceptable limit. Comparison of Fig. 3(a) (the reference model) with Figs 3(b–f) shows that the rough interface creates a spatially random de-phasing of the incident wavefield and that the de-phasing increases as the surface height distribution function, $h(x, y)$, increases from 10 m to 120 m. The principal effect of the interaction between the random rough surface and the incident wavefield is the transformation of a part of the incident energy into random noise which is delayed on the section and forms the random, incoherent part below 0.6 s. This results from the spatial convolution of the incident wavefield with the random function describing the surface height distribution. According to the Fourier theorem, if the function $h(x, y)$ describing the interface distribution is random, then the scattering pattern of the wavefield can also be described as a random distribution (de Coulon 1996). In general, the phase dependence or the effects of a signal can be nullified by computing the envelope (instantaneous amplitude) of the analytic signal by the Hilbert transform of such a signal. This permits a better visualization of the de-phasing effect on the computed data. Figure 4 shows the computed envelope of the data for the reference model and the models with surface heights from 10 m to 120 m, while Fig. 5 shows the computed phase spectra. The de-phasing is clearly evident on these plots, especially looking closely at the response of the scattering interface. The phase scattering increases with increasing surface height for a given correlation length. The computed phase spectra of the data also corroborate this observation (Fig. 5). Even for a surface height of $h(x, y) = 20$ m, which corresponds to the threshold limit of $\lambda/10$, the phase scattering can already be seen and the observed de-phasing is not negligible (Figs 3c and 4c).

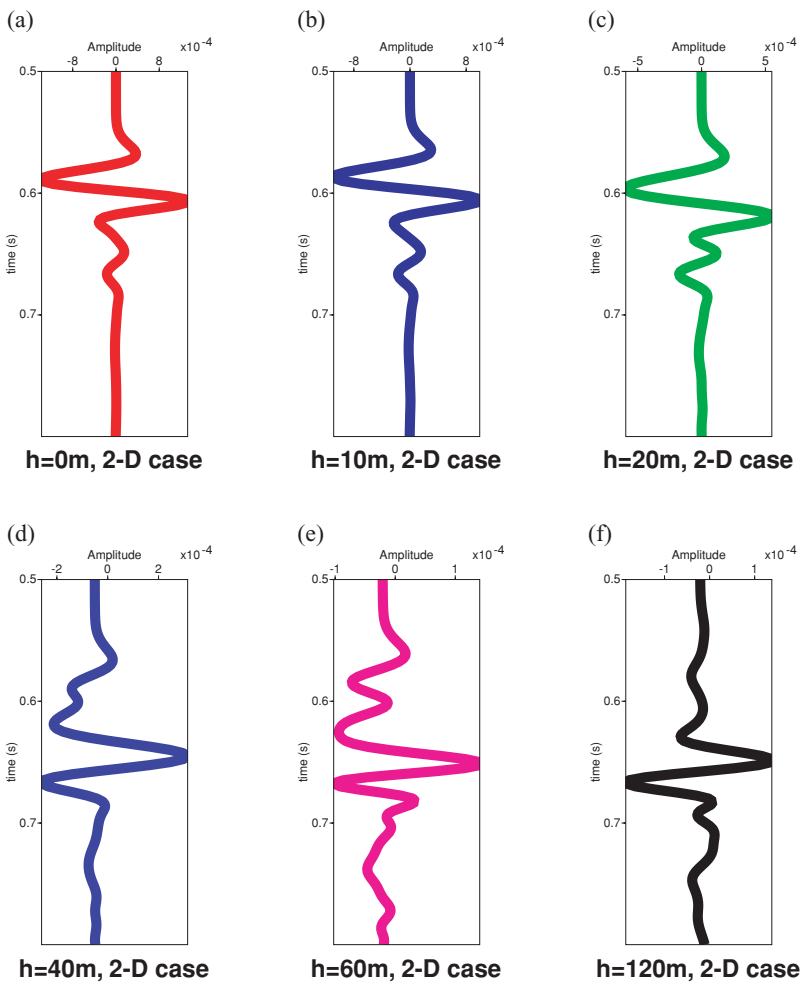

Figure 16 Stacked traces of the 2D data of Fig. 14. Note that the phase scattering is less pronounced.

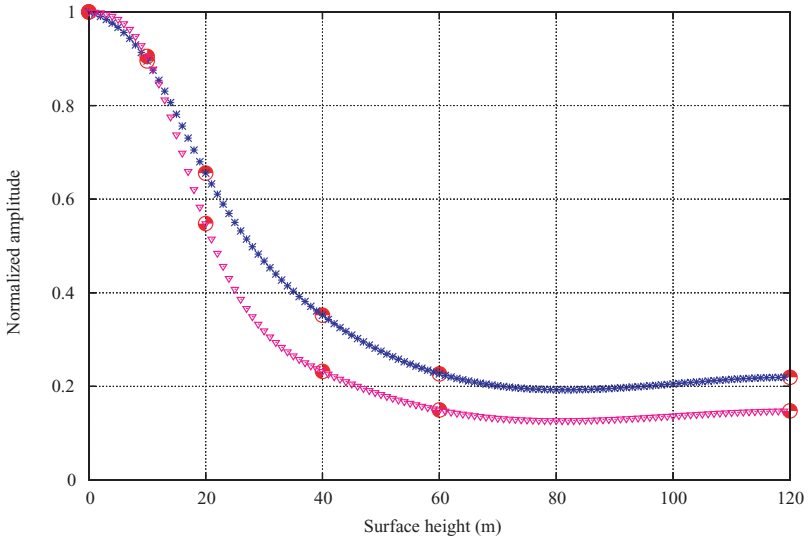

Figure 17 Normalized amplitude as a function of surface height for the synthetic data computed on the 3D (purple) and the 2D (blue) models with different surface heights. The amplitude reduces from unity to a minimum between surface heights of 40 m and 60 m, corresponding to $\lambda/5$ and $\lambda/4$, respectively.

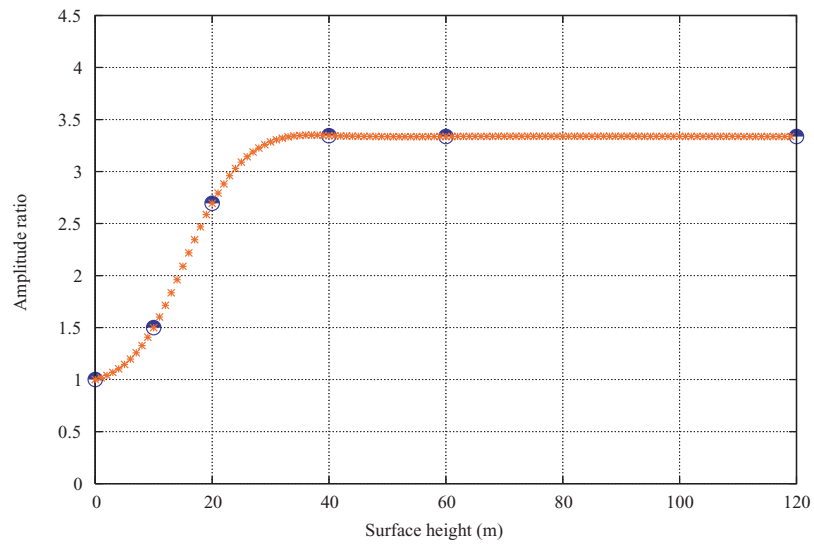

Figure 18 Ratio of the normalized amplitude of 3D and 2D data as a function of surface height. The amplitude increases from unity to about 3.4 and then remains constant.

To demonstrate the de-phasing effect qualitatively, we concentrate on the seismic response from the second interface. This interface is a perfect reflector in the reference model and a scattering reflector in the other models. A moveout correction was then applied to flatten the events for all the offset range for this interface, using exact velocity information (Fig. 6). The reflection from this interface occurs at about 0.6 s two-way traveltime (TWT) for the reference model (Fig. 6a). Figures 6(b–f) show the results for the models with surface rms heights of 10 m, 20 m, 40 m, 60 m and 120 m, respectively. The simulation on the model with a surface rms height of 10 m was carried out to show the phase evolution between the reference model, $h(x, y) = 0$, and the model with a surface height of 20 m which corresponds in our case to the Rayleigh threshold limit for a smooth interface. It was, however, observed that over all the offset range, the phase scattering is totally negligible and that there is no time delay on the recorded signal for this height. This, however, is not true as the surface height function increases from 20 m to 120 m (Figs 6c–f). For this range of the surface height function, the reflection gradually disappears from 0.6 s TWT for increasing surface height, as the incident seismic energy is converted to the scattered energy that appears at a delayed time on the section. As the surface height function increases, the phase scattering becomes more pronounced.

To facilitate the comparison of the de-phasing effect with the reference model in the 3D situation, we computed the semblance panels on the envelopes between the reference model and each set of computed data for the different surface heights. The semblance coefficient on the envelope can give a measure of similarity or semblance between two panels. If the envelopes of two given panels are respectively E_1 and E_2, the semblance on the envelopes can then be defined by the following equation:

$$S = \frac{(E_1 + E_2)^2}{2\left(E_1^2 + E_2^2\right)}. \tag{13}$$

This quantity lies between 0.5 and 1.0. A value of 0.5 means that there is no similarity between the two quantities being compared, while a value of 1.0 means equality of the compared quantities. Figure 7(a) shows the semblance on the envelope of the reference model and itself. On this figure the semblance coefficient is 1.0 as expected. Figures 7(b–f) show the semblance on the envelope of the reference model and the other models with surface heights of 10 m, 0–20 m, 0–40 m, 0–60 m and 0–120 m, respectively. The upper part of each figure has a semblance of unity as this part, comprising the direct arrival and the response of the first interface, is identical for the reference model and all the scattering models. The lower part from 0.6 s TWT, which is a measure of the scattered energy for each model compared with the reference model, has different semblance values. This corroborates the earlier observations of increasing phase scattering with increasing surface rms height which is not negligible for $\lambda/10$ (i.e. for $h(x, y) = 20$ m). Further results of the spectral analysis for the reference and the scattering models are summarized in Tables 1 and 2, respectively. These results show that the spectral bandwidth of the signal is generally reduced after scattering and that the spectral eccentricity of the signal is significantly affected. Spectral eccentricity is defined as the degree of symmetry or skewness of the amplitude spectrum of a signal. For example, zero-phased

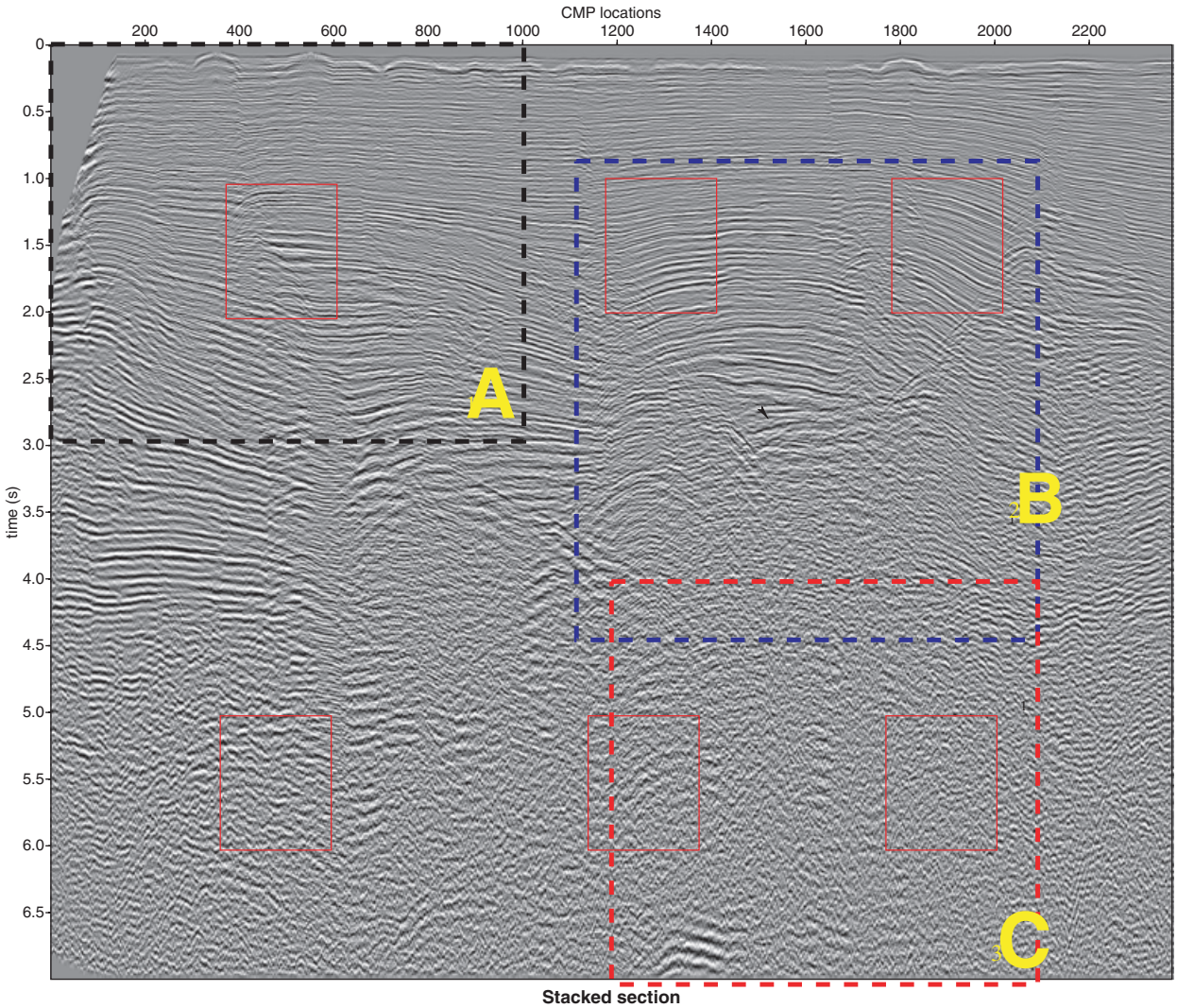

Figure 19 Real data example from offshore Niger Delta, off the West African coast. On this stacked section, the zones in the dotted boxes are explained in the text. The red boxes show the time windows used for the spectral analysis.

signal has a symmetrical amplitude spectrum and thus zero spectral eccentricity.

Figures 8 , 9 and 10 show snapshots of the wave propagating in the 3D medium at various time-steps in the (x, y)-plane below the source for the model with a surface height of 40 m. The wavefield is then described at different times before and after passing through each interface in the 3D medium. Propagating through the first interface which is a smooth surface, the wavefront remains spherical and in-phase and hence its slice is circular (Fig. 8d). On reaching the scattering interface, the wavefront loses its sphericity and its phase becomes affected (Fig. 9c). Passing through the scattering interface, the wavefront sphericity is completely lost and the phase now becomes random (Fig. 10). One part of the incident energy is strongly backscattered while the other part is transmitted through the scattering interface. The transmitted scattered wave will become further scattered in the upgoing direction, leading to further loss of phase information. The backscattered energy is usually stronger than the transmitted scattered energy, with respect to the reflection. The ratio of the transmitted to the scattered energy is a few percent; however, the ratio of the backscattered to the reflected energy is of the order of 1. Consequently, a scattering effect will occur on a stacked section and neglecting it will lead to significant errors in the quantitative interpretation of the reflection amplitude.

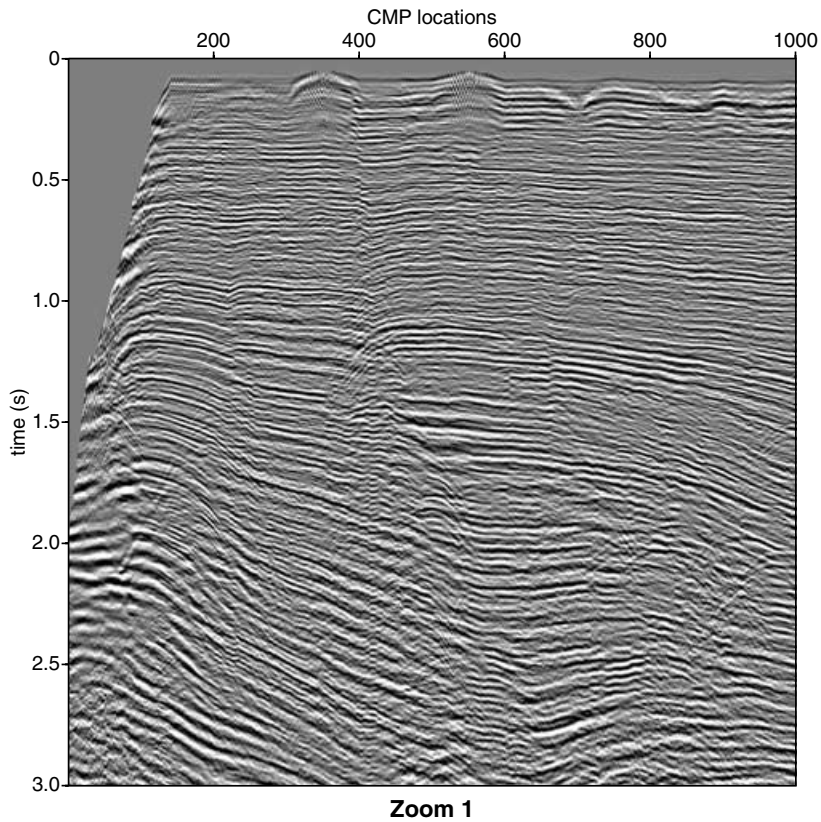

Figure 20 Zoom of zone A (black dotted box in Fig. 19). Note the good signal-to-noise ratio and the good phase fidelity of this part of the image above the scattering interface.

2D case

The equivalent 2D models used for the 2D simulations were slices of the 3D models in the (x, 0, z)-plane. The acoustic properties are thus identical to those of the 3D models. Taking the slice of the 3D model in any azimuthal direction would not affect the result as the surface distribution is independent of azimuth. Figure 11 shows such a model for a surface height of 40 m. A line source was used, resulting in circular wavefront propagation as opposed to a point source that generates spherical wavefronts for the 3D simulations. Figures 12 and 13 represent the computed data and their computed envelopes, respectively, while Fig. 14 describes the response of the second interface after moveout correction with exact velocity information. The conclusions concerning the results from the 2D simulations are identical to the results obtained for the 3D simulations: i.e. the phase scattering effect increases with increasing surface height function.

2D versus 3D

Simulations run on the equivalent 2D models show that the phase scattering effect observed is not the same as that in the 3D case. This can be better observed in Figs 6 and 14, which represent the response of the scattering interfaces in both scenarios. On the one hand, Fig. 6, which depicts simulations on the 3D models with surface rms heights of 0 m, 10 m, 20 m, 40 m, 60 m and 120 m, shows, with increase in surface height, a faster attenuation of the primary arrival at 0.6 s TWT, more pronounced scattered energy, as is evident from the generated random noise, and a more significant delay of the coda waves, as shown by the arrows on the figures. On the other hand, Fig. 14, which represents the results of the 2D simulations for the same surface height range as that of the 3D case, shows a less pronounced attenuation of the event at 0.6 s, less random noise and a continuation of the phase of the event. As an example, this event completely loses its continuity at a surface height of 40 m for the 3D case, whereas continuity is observed for the same event up to a surface height of 120 m for the 2D case.

Calibration of the scattered amplitude

In order to compare the effect of the 3D and 2D rough interfaces on the seismic section, we need to calibrate the amplitude of the events in the two cases. For this procedure, only the seismic response of the scattering surface is necessary for

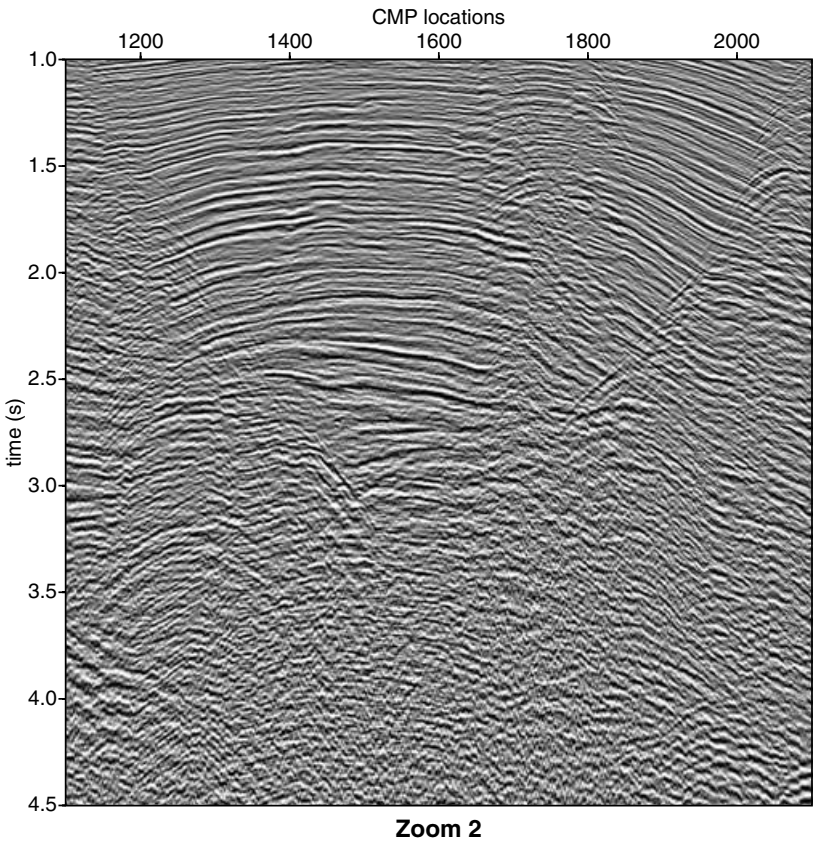

Figure 21 Zoom of zone B (blue dotted box in Fig. 19). Transition at the scattering interface.

the computations, as the direct arrival and the response of the first interface are the same for the reference and scattering models, as shown on the semblance calculation (Fig. 7). These extracted responses within a sufficient time window (Figs 6 and 14) were corrected for geometrical spreading after the moveout correction, with exact velocity information. The geometrically corrected data are stacked to obtain a single trace for each simulation. The stacked traces for the 3D and 2D simulations, shown respectively in Figs 15 and 16, corroborate the earlier observations that the phase scattering is stronger in the 3D case than in the 2D case. This is evident from the more pronounced coda waves and time delay of the interface response in the 3D case. The maximum amplitude on the envelope of the analytic signal of each stacked trace was determined and plotted as a function of the surface height (Fig. 17) after normalization with the amplitude of the reference trace for both cases. The curve associated with the normalized amplitude exhibits a Gaussian shape with decreasing values starting from 1.0, corresponding to the normalized amplitude with respect to the reference model, and reaching a minimum between surface heights of 40 m and 60 m, which correspond approximatively to $\lambda/5$ and $\lambda/4$, respectively. This attenuation is, however, stronger in the 3D case than in the 2D case. The Gaussian shape of the curve is related to the statistics of the surface distribution function. The ratio of the normalized 3D to 2D amplitudes was also computed and plotted versus the surface height function (Fig. 18). This curve shows the increase in the 3D/2D normalized amplitude ratio from unity for the reference model to a maximum of 3.4 at a surface height of 40 m; the ratio of the amplitudes then becomes constant with increasing surface height.

Consequently, for a given interface roughness height in the 3D situation, an interface roughness height of at least three times higher is required to produce an equivalent scattering effect in the 2D situation for a given correlation length of the surface distribution. This interesting result has to be kept in mind when 2D simulations of wave propagation in media with rough interfaces are realized.

Real data example

In this section, we briefly introduce the interface scattering phenomenon encountered in real situations and its effect on the final seismic image quality. Figure 19 illustrates

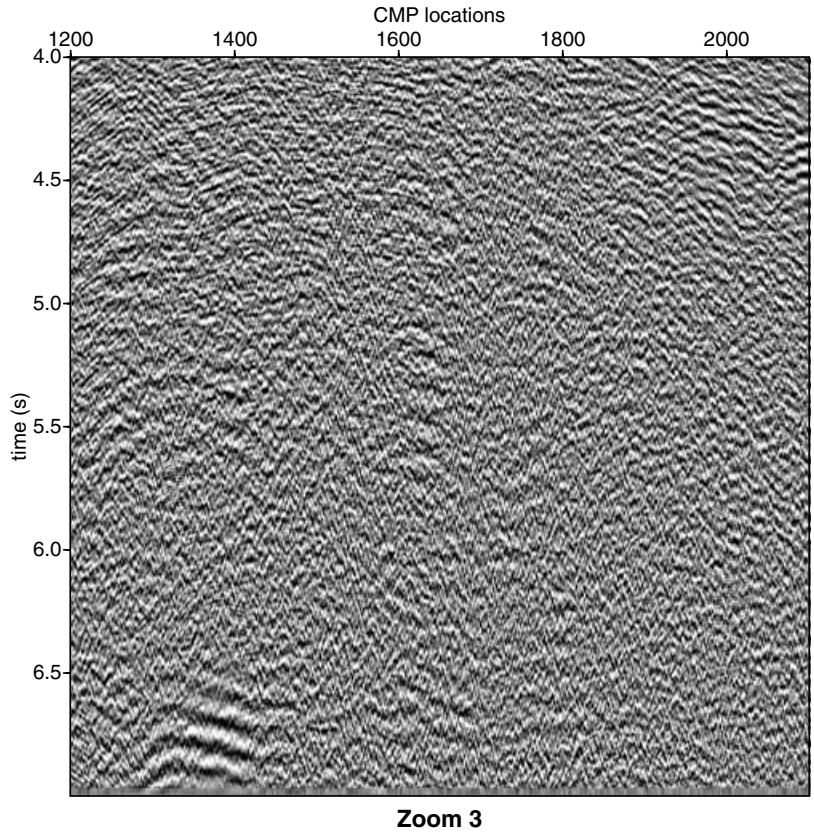

Figure 22 Zoom of zone C (red dotted box in Fig. 19). Note the poor phase fidelity as the events become random below the scattering interface.

Table 3 Spectral characteristics of the CMP time window for CMP range 400–600

Parameters	CMP 400–600 upper	CMP 400–600 lower
Frequency limits (Hz)	6.61–69.87	5.74–48.76
Carrier frequency (Hz)	38.57	26.93
Spectral eccentricity	-1.06×10^{-2}	1.49×10^{-2}
Spectral bandwidth	63.26	43.03
Signal-to-noise ratio (dB)	17.01	2.07

Table 4 Spectral characteristics of the CMP time window for CMP range 1200–1400

Parameters	CMP 1200–1400 upper	CMP 1200–1400 lower
Frequency limits (Hz)	6.60–77.11	5.70–52.36
Carrier frequency (Hz)	42.07	29.67
Spectral eccentricity	-6.13×10^{-3}	-2.75×10^{-2}
Spectral bandwidth	70.51	46.65
Signal-to-noise ratio (dB)	18.76	−1.59

a real seismic section from the offshore Niger Delta, off the West African coast. This section was obtained in a part of the region where gravity sliding and shale tectonics dominate the structural styles. The interaction of the undercompacted, overpressured, mobile shale-bodies with encasing sand-bodies results in the creation of highly rugose interfaces between the sand- and shale-bodies. Three zones can be identified in Fig. 19, shown by the dotted boxes: the upper short time zone (A), characterized by a good signal-to-noise ratio and good phase fidelity (Fig. 20); a transitional zone (B), which also describes the limit of the rugose surface as corroborated from well data (Fig. 21); and the lower part (C) below the rugose interface, which is generally characterized by very poor signal-to-noise ratio (Fig. 22). A signal-to-noise-ratio interface scattering effect dominates below the transition. It randomizes the phase of the signal and converts part of the incident seismic energy into random noise, which eventually masks the reflections from the underlying reflectors. Spectral analysis was carried out at three different CMP time windows each spanning 200 CMPs along the stacked section. Different time windows were used at locations above and below the sand/shale interface. The signal-to-noise ratio within these windows was also evaluated. Tables 3, 4 and 5 summarize the results of the spectral analysis for the CMP time windows. The frequency

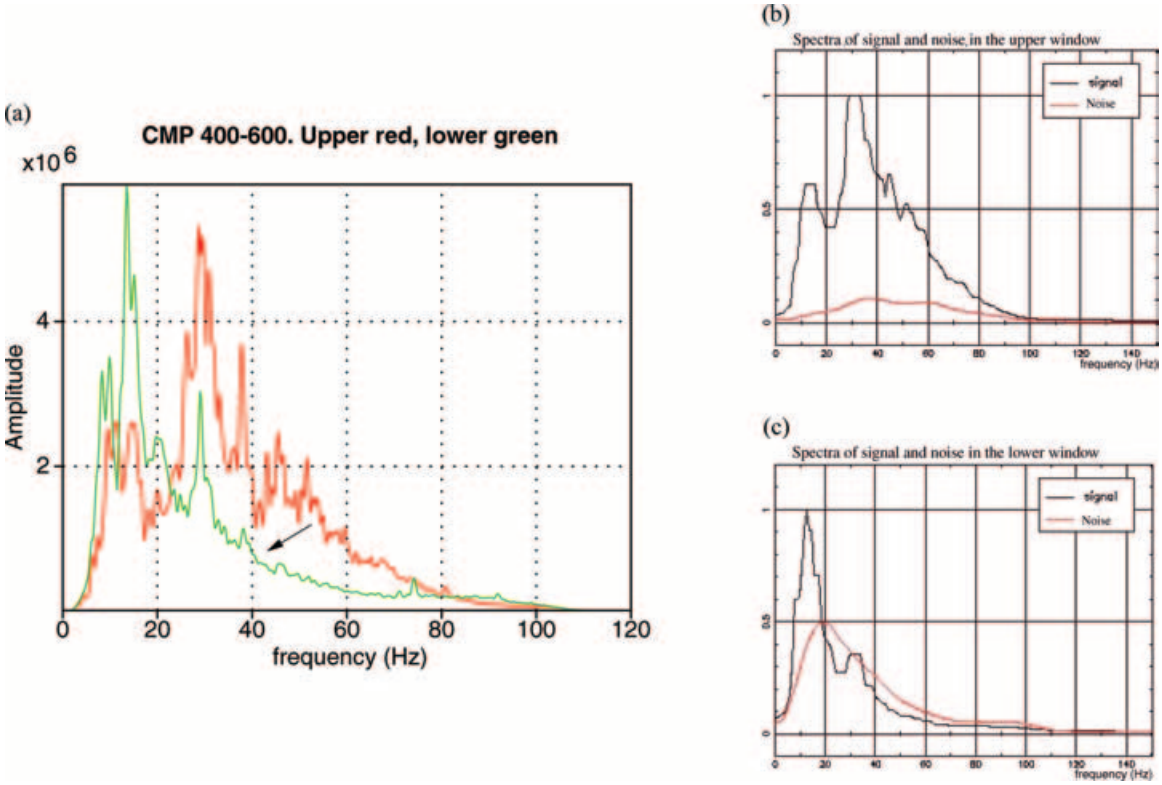

Figure 23 Spectral analysis of the real data: (a) spectra of the upper (red) and the lower (green) windows of CMP range 400–600 shown in Fig. 19. Note the reduction in the high-frequency content across the scattering interface; (b) spectra of the signal (black) and noise (red) in the upper window and (c) in the lower window. Note the considerable increase in the noise in the lower window.

Table 5 Spectral characteristics of the CMP time window for CMP range 1800–2000

Parameters	CMP 1800–2000 upper	CMP 1800–2000 lower
Frequency limits (Hz)	6.56–76.30	5.74–53.73
Carrier frequency (Hz)	42.53	31.82
Spectral eccentricity	-3.13×10^{-2}	-8.73×10^{-2}
Spectral bandwidth	69.73	47.98
Signal-to-noise ratio (dB)	19.95	−3.79

bandwidth was reduced from 63 Hz to 43 Hz for CMP range 400–600, from 71 Hz to 47 Hz for CMP range 1200–1400 and from 70 Hz to 48 Hz for CMP range 1800–2000, representing a reduction of between 40 and 48%. The lower frequencies in the frequency range do not change significantly between the time windows for each CMP range, whereas the higher frequencies are reduced, denoting the attenuation of the high frequencies as the wave passes through the scattering interface. These time windows are shown as red boxes in Fig. 19. The results of the spectral analysis are illustrated graphically in Figs 23 , 24 and 25 for CMPs 400–600, 1200–1400 and 1800–2000, respectively. These figures show the computed spectra of the upper time window (above the interface) and the lower time window (below the interface), together with the spectra of the signal and the noise. Noise is defined as the part of the signal that is not laterally correlated. The determination of this non-laterally correlated signal can be obtained by aligning the traces and determining the maxima of their intercorrelations. The average of the intercorrelation gives the signal while the average of the autocorrelation will give the signal and noise. The noise can then be obtained by subtracting the average of the intercorrelations from that of the autocorrelations. In general, the signal-to-noise ratio is drastically reduced between the time windows for all the CMP time windows as shown in Tables 3 , 4 and 5. High-frequency attenuation of seismic waves has earlier been identified and attributed to propagation effects, for example, due to absorption and thin-layer filtering (O'Doherty and Anstey 1971). It has also been shown to be progressive and global in such a case. In the case of a rugose interface, the observed attenuation is local and severe, occurring

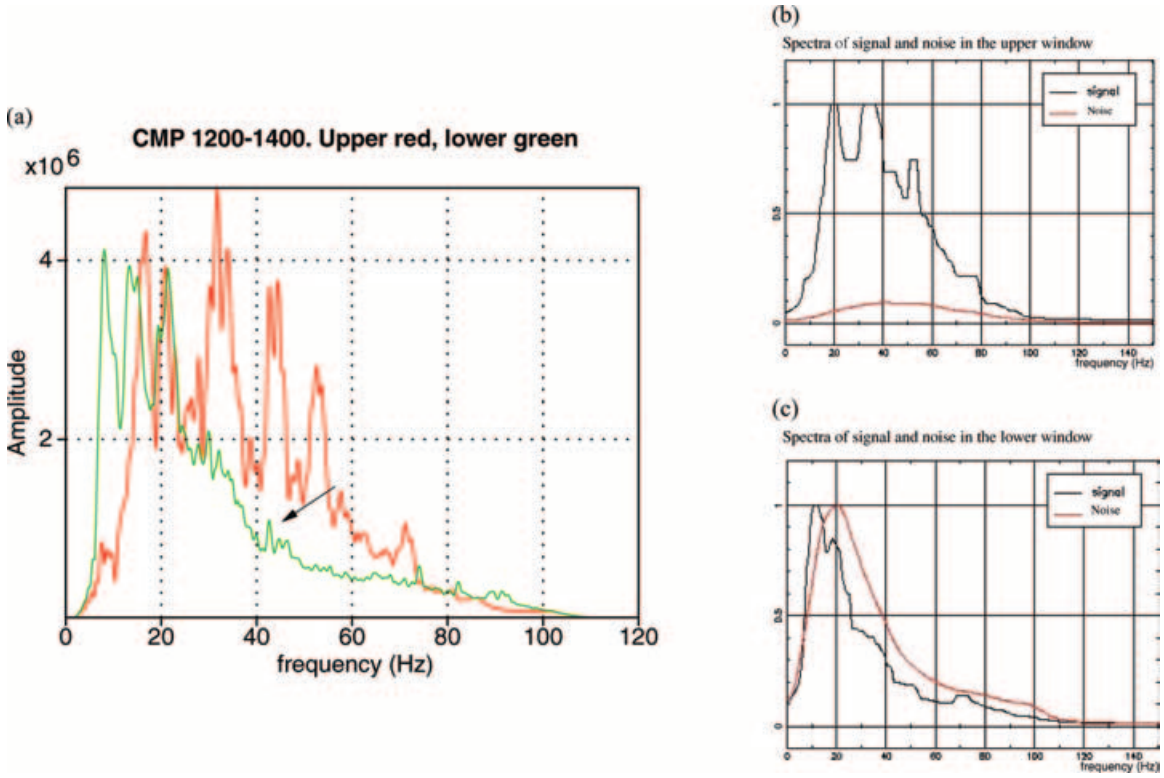

Figure 24 Spectral analysis of the real data: (a) spectra of the upper (red) and the lower (green) windows of CMP range 1200–1400 shown in Fig. 19; (b) spectra of the signal (black) and noise (red) in the upper window and (c) in the lower window. Note the total contamination of the signal by the noise in the lower window.

when the wavefield passes through the interface. This could be attributed to the multiple scattering effect, a mechanism by which the wavefield loses its high-frequency content as it is multiply scattered by the surface. Wavelengths shorter than or within the range of the surface height are mostly affected. Preservation of the lower and upper limits of the frequency spectrum (high and low frequency contents) is necessary for distinguishing the details on a seismic image. The loss of high-frequency content thus results in the loss of fine detail on a seismic image.

CONCLUSION

The main objective of this work was to investigate the effect of the interface scattering phenomenon on the seismic wavefield. Many previous studies carried out on different aspects of the problem have been restricted to 2D or 2.5D situations. Because interface scattering is a 3D phenomenon, we study the wave scattering from a randomly rough interface in a 3D configuration.

Using a finite-difference scheme in a 3D acoustic domain, we have described the effect of a random rough interface on the incident wavefield. In particular, we have shown that the interface scattering phenomenon results in the conversion of a part of the incident energy into scattered energy which is manifested as random noise, generally delayed after the reflected energy. We have also demonstrated that this effect increases with increasing surface height and becomes significant when the surface height attains 1/5 to 1/4 of the wavelength of the incident wave for a given correlation length. This phase scattering results from the spatial convolution of the incident wavefield with the function describing the surface height distribution. Consequently, the interface scattering response is not the same in 2D situations as in 3D situations; it is stronger in 3D. We have shown that surface heights that are approximately three times higher in the 2D case than in the 3D case are required to produce an almost equivalent scattering dephasing effect of the wavefield in the 2D and 3D situations. Consequently, the restriction of studies to 2D or 2.5D configurations results in the use of models that are not geologically

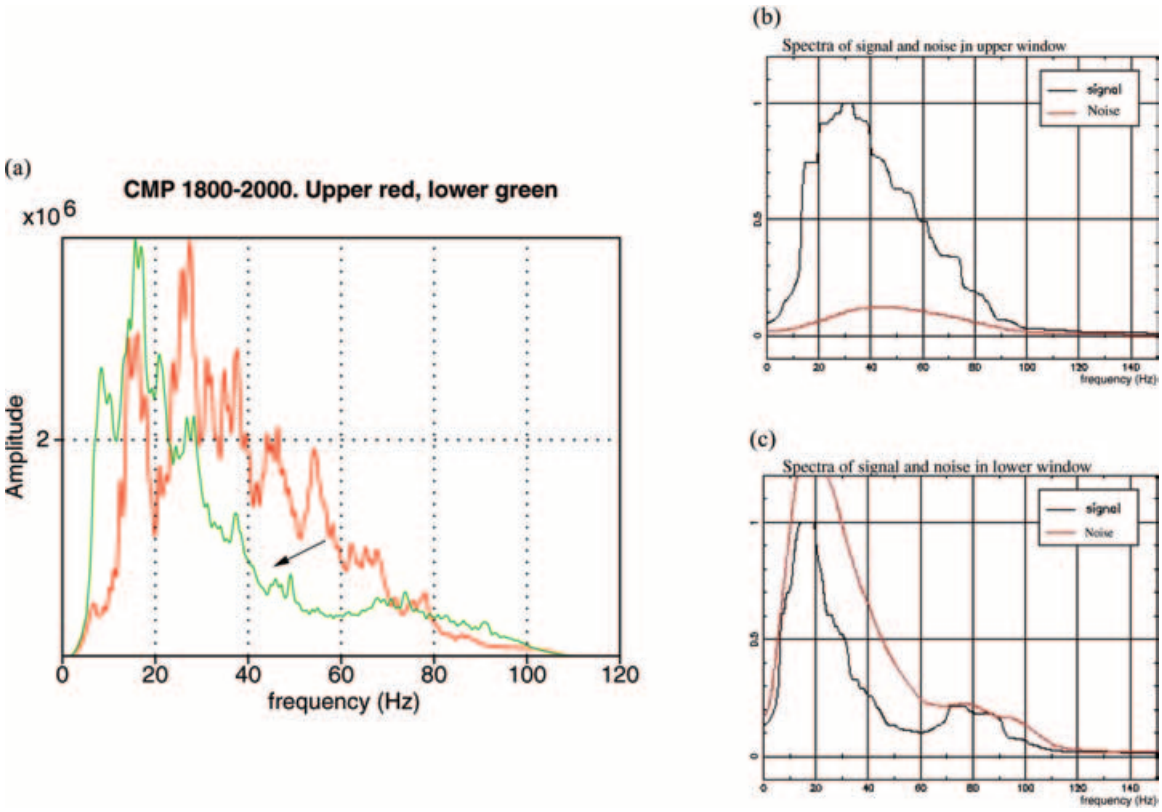

Figure 25 Spectral analysis of the real data: (a) spectra of the upper (red) and the lower (green) windows of CMP range 1800–2000 shown in Fig. 19; (b) spectra of the signal (black) and noise (red) in the upper window and (c) in the lower window. Note the total contamination of the signal by the noise in the lower window.

realistic and in an inappropriate modelling of the interface scattering phenomenon.

On real data, we have shown that seismic events resulting from interface scattering generally lose their high-frequency content due to multiple scattering, and hence contain more lower frequencies than reflected events. Finally, we have shown that the ratio of the backscattered energy to the reflected energy is high, which implies that an interface scattering effect will always be present on a stacked section in complex regions where rugose interfaces are present. Interface scattering of seismic wavefields occurs in nature in the presence of rugose interfaces with surface roughness heights of the order of the incident wavelength (order of metres). Its effect on the final seismic image is not always negligible in 3D as is often assumed, even when the surface heights are of the order of 1/10 of the incident wavefield. Consequently, this phenomenon should be critically considered when using phase information for inversion purposes, especially in geological settings where rugose surfaces are present. The interface scattering effect will be present on stacked sections but the dephasing will be proportional to the scattering surface height.

ACKNOWLEDGEMENTS

The research leading to this work was financed by Total Nigeria (EPNL), a subsidiary of the Total Group and the French Government. We are grateful to Dominique Rousset and Dimitri Komamtitsch of the University of Pau for fruitful discussions concerning the development of the 3D finite-difference code, especially on issues relating to absorbing boundaries. We thank Dr F. Martini and an anonymous reviewer for constructive criticism which helped in improving this paper.

REFERENCES

Axilrod H.D. and Ferguson J.F. 1990. SH-wave scattering from a sinusoidal grating: An evaluation of four discrete wave number

techniques. *Bulletin of the Seismological Society of America* **80,** 644–655.

Bouchon M., Campillo M. and Gaffet S. 1989. A boundary integral-equation discrete wavenumber representation method to study wave propagation in multilayered media having irregular interface. *Geophysics* **54,** 1134–1140.

Box G.E.P. and Muller M.E. 1958. A note on the generation of normal deviates. *Annals of Mathematical Statistics* **28,** 601–611.

de Coulon F. 1996. *Theorie et Traitement des Signaux*. Presses Polytechniques et Universitaires Romandes, Lausanne. ISBN 2040157786.

Favretto-Cristini N. and de Bazelaire E. 2003. PP-amplitude bias caused by interface scattering: Are diffracted waves guilty? *Geophysical Prospecting* **51,** 99–115.

Ishimaru A. 1978. *Wave Propagation and Scattering in Random Media*, Vol. 2. Academic Press. ISBN 0123747023.

Kawase H. 1988. Time domain response of a semi-circular canyon for incident SV, P and Rayleigh waves calculated by the discrete wavenumber boundary element method. *Bulletin of the Seismological Society of America* **78,** 1415–1437.

Kelly K.R., Ward R.W., Treitel S. and Alford R.M. 1976. Synthetic seismograms: A finite difference approach. *Geophysics* **41,** 2–27.

Martini F. and Bean C.J. 2002. Application of pre-stack wave equation datuming to remove interface scattering in sub-basalt imaging. *First Break* **20,** 395–403.

O'Doherty R.F. and Anstey N.A. 1971. Reflections on amplitudes. *Geophysical Prospecting* **19,** 430–458.

Ogilvy J.A. 1991. *Theory of Wave Scattering from Random Rough Surfaces*. Institute of Physics Publishing. ISBN 0750300639.

Schultz A.C. and Toksöz M.N. 1991. Seismic wave scattering from a randomly grooved interface: ultrasonic modeling and finite difference calculation. American Geophysical Union, Fall Meeting, Expanded Abstracts, S21A-03,8Z.

Schultz A.C. and Toksöz M.N. 1993. Enhanced backscattering of seismic waves from a highly irregular, random interface: SH case. *Geophysical Journal International* **144,** 91–102.

Virieux J. 1986. P-SV wave propagation in heterogeneous media: velocity stress finite difference method. *Geophysics* **51,** 889–901.

Warnick K.F. and Chew W.C. 2001. Numerical simulation methods for rough surface scattering. In: *Waves in Random Media II*. Institute of Physics Publishing. ISSN 09597174.